Argonne NATIONAL LABORATORY

ANL/CFCT-23/25

Integrated Process Testing of MSR Salt Spill Accidents

Chemical and Fuel Cycle Technologies Division, Argonne National Laboratory

ANL/CFCT-23/25

Integrated Process Testing of MSR Salt Spill Accidents

Prepared by
Sara Thomas and Josh Jackson
Chemical and Fuel Cycle Technologies Division, Argonne National Laboratory

September 15, 2023

Acknowledgements

This experimental portion of this report was produced under the auspices of the US DOE Fuel Cycle R&D program Molten Salt Reactors Campaign. Issuance of this report meets milestone M3RD-23AN0602091. The modeling portion of this report was supported by the Multiphysics Applications technical area within the US DOE Nuclear Energy Advanced Modeling and Simulation (NEAMS) program, as a recommended task to close information gaps and develop mechanistic source term analysis capabilities for advanced reactors. The authors gratefully acknowledge Ms. Yifen Tsai, Ms. Kristin DeAngeles, and Dr. Seema Naik for performing the compositional analyses discussed herein. The suggestions and discussions with participants of the MSR Campaign as well as Argonne staff including Dr. Mitchell Farmer and Dr. Shayan Shahbazi benefitted this project and are greatly appreciated.

This work was conducted at Argonne National Laboratory and supported by the U.S. Department of Energy, Office of Nuclear Energy, under Contract DE-AC02-06CH11357.

Table of Contents

Figures

Tables

Acronyms

ADDER	Advanced Dimensional Depletion for Engineering of Reactors
DSC	Differential scanning calorimetry
EDS	Energy dispersive X-ray spectroscopy
EPIC	Edge programmable industrial controller
FLiNaK	LiF-NaF-KF eutectic (46.5-11.5-42 mol %)
ICP-MS	Inductively coupled plasma-mass spectrometry
ICP-OES	Inductively coupled plasma-optical emission spectroscopy
IR	Infrared
MCNP	Monte Carlo N-Particle
MSR	Molten salt reactor
MSRE	Molten Salt Reactor Experiment
MSTDB-TC	Molten Salt Thermal Properties Database–Thermochemical
NRC	Nuclear Regulatory Commission
PTFE	Poly(tetrafluoroethylene)
SEM	Scanning electron microscopy

Abstract

Part of the licensing process for new nuclear reactors requires vendors to assess the potential consequences of identified accident scenarios using accident progression modeling. The accident scenario that will likely be evaluated by all molten salt reactor (MSR) developers is a spill of radionuclide-bearing fuel salt onto the reactor containment floor (i.e., a salt spill accident). The development of accident progression models requires experimental data to inform which processes to incorporate, to enable the calculation of parameters to model these processes, and to validate the model predictions. The data should quantify the sensitivities of key processes (e.g., molten salt spreading, heat transfer, containment structure corrosion, radionuclide vaporization, and aerosol generation) towards the initial conditions of the spill, the ambient environment, and the features of the containment. In addition, results from integrated process tests that quantify coupled processes are required to validate systems-level models.

This report documents results from integrated process tests conducted on simulated molten salt spill accidents. The generated experimental data simultaneously quantify the heat transfer behavior of the spilled salt, compositional changes to the bulk salt, and the release of surrogate fission products from the spilled salt as aerosol particles. All tests that were conducted used FLiNaK doped with surrogate fission products, and the variables that were evaluated included the initial salt temperature and the concentration of surrogate fission products present in the salt.

The major accomplishments of this work include identifying surrogate fuel salt compositions that provide insight into the dispersal behavior of radionuclides of potential significance to the source term, employing previously developed methods and measurement techniques to simultaneously measure key processes, generating data on the coupled processes of molten salt heat transfer and surrogate fission product release as aerosol particles, demonstrating new test methods for real-time monitoring of the flow rate of the spill and aerosol size quantification in an argon atmosphere, and developing a mass transport model for cesium and iodine release from molten FLiNaK to provide insight into aerosol formation by vapor condensation. The same methodology applied herein can be employed to study different salt compositions of interest to MSR developers, different environmental conditions, and other variables that are relevant to postulated accident scenarios. The insights gained from these integrated process tests conducted at a laboratory scale will be incorporated into future integral effects tests conducted at an engineering scale.

1 Introduction

Reactor safety is demonstrated to the U.S. Nuclear Regulatory Commission (NRC) in part by employing validated accident progression and mechanistic source term models to predict the consequences of postulated accident scenarios. One challenge that molten salt reactor (MSR) vendors face in developing U.S. NRC license applications is the lack of existing experimental data that quantify the consequences of postulated accident scenarios for MSRs. Experimental efforts should focus on providing technical bases to develop and validate accident progression and mechanistic source term models for postulated MSR accidents to support MSR licensing.

The most common accident scenario to be evaluated by MSR developers will likely involve a spill of molten fuel salt from the reactor vessel onto the containment floor. The processes expected to have the greatest influence on the outcome of a salt spill accident include spreading on the catch pan, heat transfer from the salt to its surroundings, corrosion and warping of the catch pan, radionuclide vaporization and condensation, and radionuclide-bearing splatter and aerosol generation (Thomas, 2023). Recent tests conducted at Argonne have demonstrated methods and measurement techniques to quantify these processes individually and to provide insights into radionuclide dispersal and bulk salt behavior during and after a molten salt spill accident (Thomas and Jackson, 2021, 2022). Tests addressing individual processes can provide the mechanistic detail that is required for model development, but results from integral effects tests are needed to quantify the coupling between the thermohydraulic behavior of the molten salt and radionuclide dispersal during a salt spill accident (Shahbazi and Grabaskas, 2021). The validation of systems-level accident progression codes (e.g., MELCOR; Humphries et al., 2018) will require experimental data generated from integral effects tests that are conducted at a large enough scale to ensure that the results are representative of full-scale accidents (Leute et al., 2021; Thomas, 2023).

This report presents the results obtained from integrated process tests designed to quantify the consequences of molten fuel salt spill accidents. These tests were conducted at a laboratory scale using two compositions of FLiNaK doped with surrogate fission products to represent low and high burnup surrogate fuel salt. The objectives of the work presented in this report were to:

- Identify surrogate fuel salt compositions to employ in molten salt spill tests that will provide insight into fission product dispersal behavior and the effect of fission products on the thermohydraulic behavior of the salt,
- Generate experimental data on coupled processes that will inform accident progression and mechanistic source term models,
- Demonstrate the application of previously developed methods and techniques to simulate and measure important processes on more complex test systems, and
- Provide the experience in measuring several processes simultaneously that will facilitate conducting integral effects tests at an engineering scale.

New measurement techniques were tested for future use in individual and integrated process tests as part of this work and are presented in Appendix A. A data package containing complete datasets for some of the results shown herein is available from the lead author upon request. The available datasets are identified in the following sections.

2 Salt composition and rationale

2.1 Depletion calculations for the MSRE

Results from recently reported fuel depletion calculations for the Molten Salt Reactor Experiment (MSRE) are presented and compared in this section to guide the selection of surrogate fission product concentrations for a surrogate fluoride fuel salt that is representative of thermal spectrum MSRs. The first set of depletion results for the MSRE were obtained from a roadmap report describing recommended salt compositions to use as surrogate fuel salt for thermal property measurements (McMurray et al., 2021). The depletion datasets in that report were generated using TRITON within the SCALE suite of reactor physics codes, and the parameters for the calculation are shown in Table 1. The SCALE-TRITON calculations were performed assuming the entire primary loop of MSRE fuel salt was a stationary and homogenous mixture and used the continuous processing capability. McMurray et al. (2021) did not state whether the SCALE-TRITON calculations included refueling or what the removal rates of specific nuclides were from the salt.

The second set of depletion results for the MSRE were recently calculated using the Advanced Dimensional Depletion for Engineering of Reactors (ADDER) software coupled with the Monte Carlo N-Particle (MCNP) transport code (Fei et al., 2022). The calculations were performed assuming that the reactor is not refueled, that the fission, transmutation, and decay products build up in the fuel salt (i.e., no processing or vaporization occurs), that corrosion products are not present, and that the reactor ran at full power (7.34 MWth) for 10 years. The parameter values used in the MCNP-ADDER calculation are reported in Table 1.

Table 1: Parameters for calculating the nuclide inventory of the MSRE using SCALE-TRITON and MCNP-ADDER depletion codes

	SCALE-TRITON (2021)	MCNP-ADDER (2022)
Fuel type	35% enriched ^{235}U	31.6% enriched ^{235}U
Starting salt composition (mole %)	65.0 LiF – 29.1 BeF_2 – 5.0 ZrF_4 – 0.9 UF_4	64.96 LiF – 29.27 BeF_2 – 4.98 ZrF_4 – 0.79 UF_4
Reactor power	Not disclosed	7.34 MWth
Operation duration (years)	10 and 30	10

The MSRE depletion results performed using SCALE-TRITON for 10 and 30 years of reactor operation and using MCNP-ADDER for 10 years of reactor operation are shown in Table 2. The nuclide contributions were summed to provide elemental concentrations, and the elemental concentrations were converted to the concentration of the anticipated most stable species of that element in the salt (except for iodine), as shown in Table 2. Only the chemical species present at the highest concentrations are listed in Table 2, and noble gases and highly volatile elements (e.g., hydrogen) are not shown. The depletion results are presented as concentration of the most stable species to enable a comparison between the different calculations and to facilitate the selection of surrogate fuel salt compositions.

Table 2: Fuel salt composition of the MSRE (mole %) predicted from depletion calculations for 10 and 30 years of reactor operation[a,b,c]

Species	MCNP-ADDER (2022) 10 years	SCALE-TRITON (2021) 10 years	SCALE-TRITON (2021) 30 years	Stream[d]
LiF	64.73	64.95	64.87	Fuel
BeF_2	29.20	29.08	29.05	Fuel
ZrF_4	5.00	5.02	5.08	Fuel
UF_4	6.74×10^{-1}	7.80×10^{-1}	5.58×10^{-1}	Fuel
Mo	1.05×10^{-2}	2.71×10^{-2}	7.89×10^{-2}	Solid waste
NdF_3	5.66×10^{-3}	2.22×10^{-2}	6.41×10^{-2}	Fuel
CsF	5.29×10^{-3}	1.97×10^{-2}	5.92×10^{-2}	Fuel + gas waste
CeF_3	3.72×10^{-3}	1.48×10^{-2}	3.95×10^{-2}	Fuel
Ru	5.03×10^{-3}	1.23×10^{-2}	4.19×10^{-2}	Solid waste
PuF_3	1.79×10^{-3}	1.23×10^{-2}	1.48×10^{-2}	Fuel
SrF_2	3.94×10^{-3}	9.87×10^{-3}	2.22×10^{-2}	Fuel
BaF_2	2.32×10^{-3}	7.40×10^{-3}	2.71×10^{-2}	Fuel
LaF_3	1.90×10^{-3}	7.40×10^{-3}	1.97×10^{-2}	Fuel
PrF_3	1.70×10^{-3}	4.93×10^{-3}	1.73×10^{-2}	Fuel
Tc	2.43×10^{-3}	7.40×10^{-3}	1.97×10^{-2}	Solid waste
I	3.11×10^{-4}	Not reported	Not reported	Not reported

[a] Concentrations are reported for the anticipated most stable species except for iodine (I), which is reported as its elemental composition.
[b] Only the species with the highest concentrations are included; results do not sum to 100 mole %.
[c] Noble gases and highly volatile elements (e.g., hydrogen) are not shown.
[d] The SCALE-TRITON model considered continuous processing and identified the elements that would remain in the fuel or be removed as solid or gas waste.

The concentrations of the top products of fission, transmutation, and decay that were calculated by SCALE-TRITON for 10 years of reactor operation are approximately two to four times greater than those calculated by MCNP-ADDER for the same duration of operation (Table 2). The differences can likely be attributed to calculations with the SCALE-TRITON model using a higher starting concentration of UF_4 (0.9 mole % versus 0.79 mole %) with a higher content of ^{235}U (35.0% ^{235}U versus 31.6% ^{235}U; see Table 1) and a different reactor power. The UF_4 concentration and ^{235}U content used in the MCNP-ADDER calculations are more consistent with the actual MSRE operation than those used in the SCALE-TRITON calculations described in McMurray et al. (2021). Thus, the depletion results reported in Table 2 that were calculated by MCNP-ADDER are likely more representative of the fuel salt inventory of the MSRE than those calculated by the original SCALE-TRITON model from McMurray et al. (2021). Depletion results from a higher-fidelity SCALE-TRITON model of the MSRE are more recently reported in Lo et al. (2022) and Bostelmann et al. (2022), but the full inventory of the fuel salt is not disclosed.

The depletion results for the MSRE calculated by the MCNP-ADDER model were compared to the results from the more recent SCALE-TRITON calculations of the MSRE (Lo et al., 2022) that were posted on GitLab (https://code.ornl.gov/scale/analysis/non-lwr-models-vol3/-/tree/master/). This comparison is described in Fei et al. (2022). The MCNP-ADDER model of the MSRE was modified for the direct comparison so that it used the same parameters and considerations as the updated SCALE-TRITON model, as described in Fei et al. (2022). The depletion results calculated by both

codes are in very good agreement. Among the top assessed 400 nuclides, the concentration difference for nearly half are within 5% and for nearly 75% are within 30% (Fei et al., 2022).

The depletion results for the MSRE that were calculated using MCNP-ADDER were also compared to the radionuclide compositions of fuel salt samples taken from the MSRE at various time points throughout its operation. To facilitate a comparison, the MCNP-ADDER calculations were repeated to simulate the power history of MSRE operation with ^{235}U fuel in 91 burn-up durations representing the intermittent power history. The depletion calculations were done for durations that matched the fuel salt sampling durations for which experimental data are available. The calculated depletion results are in good agreement with the measured data for salt-soluble nuclides (Fei et al., 2022). Greater discrepancies are seen between the experimentally measured and calculated salt concentrations of nuclides with noble gas precursors and semi-volatile elements (e.g., iodine and cesium) because the calculations did not account for loss due to vaporization.

2.2 Surrogate fuel salt compositions for testing

Two surrogate fuel salt compositions were used in tests to provide insight into the dispersal behavior of key radionuclide species due to a molten salt spill accident for an MSR. The two compositions have different concentrations of the same chemical species that simulate a low and high burnup fuel salt and are presented in Table 3.

Table 3: Compositions of surrogate fluoride fuel salt (mole %)

Component	Composition 1 (low burnup)	Composition 2 (high burnup)
FLiNaK	99.645	98.225
ZrF_4	0.05	0.25
Mo	0.05	0.25
NdF_3	0.05	0.25
CeF_3	0.05	0.25
CsF	0.05	0.25
CsI	0.005	0.025
SrF_2	0.05	0.25
Ru	0.05	0.25
Te[a]	0.005	0.025

[a] Added as Na_2Te

The salt compositions were simplified from the compositions provided by the depletion calculations by selecting surrogate fission products to represent those with similar expected chemical behavior. The surrogate fuel salt compositions use FLiNaK as the base salt and exclude actinides (e.g., UF_4). The concentration of ZrF_4 is intended to represent the zirconium that would be present in the salt as a fission product rather than as a fuel salt additive, as was done for the MSRE. Molybdenum represents the elements that can exist as metallic or fluoride species depending on the redox potential of the salt (e.g., Mo and Tc). NdF_3 is the trivalent rare earth metal of highest concentration according to the depletion results (Table 2) and represents all trivalent rare earth elements. CeF_3 represents the rare earth metals that can exist in trivalent and tetravalent oxidation states (e.g., Ce and Pr) and is also used as a surrogate for PuF_3. Cesium and iodine are included in the composition because they are particularly significant to source term assessments due to the contribution of their isotopes to dose consequence (e.g., ^{137}Cs and ^{131}I) and the relatively high

vapor pressures of cesium- and iodine-bearing species above fluoride salts. Cesium and iodine are added as CsF and CsI to yield a cesium to iodine ratio of approximately 10 to 1, which approximately matches the depletion results shown in Table 2. Maintaining a realistic ratio of cesium to iodine is important because the ratio can influence the formation of CsI, which is known to be volatile when present in fluoride salts. Tellurium is included in the salt compositions (as Na_2Te), although it is not one of the major fission products in terms of yield, due to uncertainties in its chemical and transport behavior, the radiotoxicity of its isotopes, and the fact that ^{131}Te is the precursor to ^{131}I. Finally, SrF_2 represents the alkaline earth metals of significance (e.g., SrF_2 and BaF_2), and Ru represents the noble metals.

The actual composition of the fuel salt of a specific MSR design at a given time will depend on many factors including the reactor power level, fissile composition of the fuel salt, the duration of operation, and the loss rate of nuclides due to processes like vaporization and decay. Surrogate fission product compositions were selected to provide insights into radionuclide dispersal that are relevant to all MSR concepts and not to mimic the fuel composition predicted for a particular MSR design. For this reason, the two surrogate fuel salt compositions each contain equal mole fractions of the surrogate fission products. One exception is that the concentration of CsI is 10 times lower than the CsF concentration. The other exception is Na_2Te, which is added at a concentration that is 10 times lower than the other surrogate fission products due to a lower expected fission yield. The concentration of each surrogate fission product is five times higher in Composition 2 than in Composition 1. This should allow an MSR developer to extrapolate the results generated from the two compositions of this work to any composition of interest.

The concentrations of individual surrogate fission product species for the low burnup composition (Composition 1 in Table 3) fall within the concentration bounds of the three sets of depletion results shown in Table 2. In contrast, the surrogate fission product concentrations for the high burnup composition (Composition 2 in Table 3) are higher than those of the most conservative set of depletion results (30 years of MSRE operation). These higher concentrations were chosen for the high burnup composition to increase the likelihood that the elements will be detected during testing using the analysis techniques described in Section 4.2. Additionally, the mole fractions of surrogate fission products in the high burnup composition are higher than the mole fractions in the depletion results to be more representative of commercial MSRs, which will likely feature power levels around an order of magnitude higher than the roughly 8 MWth MSRE.

The salt compositions in Table 2 were used to investigate the effects of fission product presence on the thermophysical and thermochemical properties of a fuel salt (phase behavior, heat capacity, and thermal diffusivity), and the results are provided in Gardner and Rose (2023).

3 Salt preparation

All reagents used in the synthesis of FLiNaK and as surrogate fission products had a purity of > 99.9% except for the KF, which had a purity of > 99%. Reagent preparation, salt synthesis, and salt sample preparation were conducted in an argon atmosphere glovebox (O_2 < 10 ppm, H_2O < 1 ppm). Upon receipt, the salt reagents were transferred to the glovebox and were individually heated in nickel crucibles to remove adsorbed water and volatile impurities. The NaF, KF, LiF, NdF_3, CeF_3, SrF_2, and ZrF_4 powders were heated at 300 °C for at least four hours and then at 700 °C for at least eight hours. The CsF and CsI powders were heated at 300 °C for 12 hours. The molybdenum (Mo), ruthenium (Ru), and Na_2Te reagents were not heated in a furnace prior to their addition to FLiNaK as surrogate fission products. The nickel crucibles used to bake out reagent powders and in the salt synthesis were custom made and cleaned with soap and water, manually

polished with steel wool, and then cleaned with methanol and lint-free wipes to remove oxide residue. The nickel crucibles were baked out at 700 °C for at least four hours prior to their use.

Approximately 700 g of eutectic FLiNaK was synthesized in three batches. Appropriate amounts of the reagents were added directly to the nickel crucible to achieve the eutectic composition (46.5 mol % LiF, 11.5 mol % NaF, and 42.0 mol % KF), mechanically mixed, and then heated to 700 °C for at least eight hours to fuse the salt. The as-batched compositions of the three FLiNaK batches are provided in Table 4. Each of the three fused salt batches were crushed and combined into one large single batch that was then fused at 700 °C, allowed to cool, and crushed a second time to homogenize the salt mixture. The molar composition of the final batch of synthesized FLiNaK was calculated from the batched masses and is provided in Table 5. An aliquot of the final batch of synthesized FLiNaK was heated in a nickel crucible in a furnace to 700 °C and subsequently removed from the furnace and allowed to cool. A cooling curve of this aliquot was measured by using an infrared camera to confirm the expected freezing temperature prior to doping the FLiNaK with surrogate fission products for use in salt spill testing (data not shown).

Table 4: As-batched compositions of synthesized FLiNaK

Batch number	Mass LiF (g)	Mass NaF (g)	KF (g)
1	67.197	26.868	135.854
2	67.104	26.870	135.885
3	67.191	26.890	135.908
Sum	201.492	80.628	407.647

Table 5: Calculated molar composition of FLiNaK

	LiF (mol %)	NaF (mol %)	KF (mol %)
Calculated	46.5	11.5	42.0
Target	46.5	11.5	42.0

The two compositions of FLiNaK salt containing surrogate fission products were made by directly adding prescribed amounts of the crushed pure FLiNaK and dried (as appropriate) powdered reagents to the graphite crucible used in spill tests. Specifically, approximately half of the desired amount of FLiNaK was added to a graphite crucible first. The surrogate fission product powders were added above this first FLiNaK layer and then the remainder of the FLiNaK was added above the surrogate fission product powders. The surrogate fission product powders were intentionally sandwiched between layers of FLiNaK in the crucible to promote mixing and reduce the vaporization of surrogate fission product species during heating in the furnace. The FLiNaK and surrogate fission product reagent mixtures were heated for at least 16 hours prior to pouring in spill tests. The graphite crucibles in which the FLiNaK was mixed with the surrogate fission product reagents were designed so that they could be manually removed from a furnace with crucible tongs. The graphite crucibles were wiped with methanol and baked out at 700 °C for at least four hours prior to use.

The batched compositions of the low burnup and high burnup surrogate fuel salts are presented in Table 6. Aliquots taken from the salt after it was spilled were analyzed for elemental composition by using inductively coupled plasma-optical emission spectroscopy (ICP-OES) and inductively coupled plasma-mass spectrometry (ICP-MS). The measured elemental composition results are presented for each test in Section 5.7. Images of frozen samples of the synthesized low and high

burnup FLiNaK are shown with pure FLiNaK for comparison in Figure 1. Both the low burnup and high burnup FLiNaK are a purple-gray color, and the high burnup FLiNaK is a darker shade than the low burnup FLiNaK.

Table 6: Batched masses (g) of low and high burnup surrogate fuel salt components

Reagent	Low burnup	High burnup
FLiNaK	316.015	299.973
ZrF_4	0.634	3.06
Mo	0.364	1.734
NdF_3	0.792	3.69
CeF_3	0.742	3.649
CsF	0.587	2.799
CsI	0.117	0.476
SrF_2	0.473	2.356
Ru	0.379	1.862
Na_2Te	0.081	0.316
Sum	320.184	319.915

Figure 1: Frozen samples of synthesized pure, low burnup, and high burnup FLiNaK

4 Integrated process test description and methods

Methods to quantify processes important to the consequences of an MSR salt spill accident were developed previously using a fluoride salt (Thomas and Jackson, 2021) and a chloride salt (Thomas and Jackson, 2022). For the work described herein, these methods were integrated to simultaneously monitor processes during a simulated molten salt spill accident in a laboratory.

4.1 Design and description of test equipment

All tests described in this report simulated a salt spill scenario in which molten salt spills from a vessel into an insulated cylindrical catch pan and forms a static pool. This scenario is depicted in Figure 2, which identifies the consequence-determining processes that require quantification. Methods were employed to simulate the molten salt spill scenario depicted in Figure 2 in laboratory-scale tests to measure the integrated effects of molten salt impaction onto the catch

pan surface, molten salt cooling and heat transfer to its surroundings, and surrogate fission product disperal.

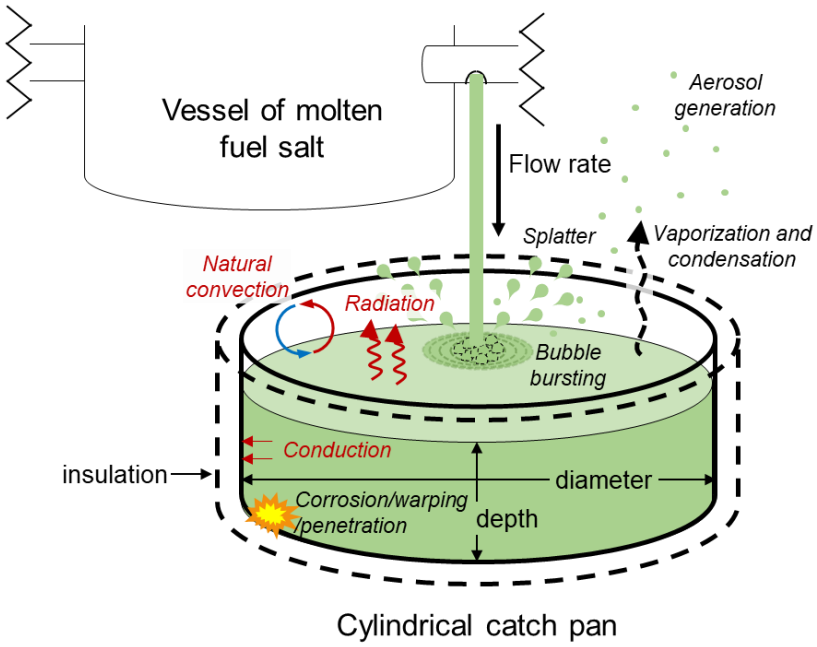

Figure 2: Schematic of molten salt spill scenario being simulated in laboratory-scale integral effects tests.

Figure 3A presents a schematic of the test system and identifies the location of measurement equipment and Figure 3B shows a photograph of the test system in the argon atmosphere glovebox. All tests were conducted under an argon atmosphere (O_2 < 10 ppm, H_2O < 1 ppm). The FLiNaK doped with surrogate fission products was first heated in a graphite crucible within a furnace to the target temperature and then manually poured through the pour inlet of a stainless steel containment box and into a 316 stainless steel beaker using long crucible tongs (Figure 3B).

The base of the stainless steel containment box has dimensions of 12 in. × 12 in. × 12 in. (L × W × H) and is the same structure that was used to contain molten salt splatter and aerosols during previously conducted molten salt splashing tests (Thomas and Jackson, 2021, 2022). A custom-designed “roof” was added to the base of the containment box, which holds the IR and visible cameras and includes an inlet for pouring molten salt into the box (Figure 3B). The pour inlet is wide enough so that the stream of molten salt does not contact the inlet walls while it is being poured into the box.

The 316 stainless steel beaker that was used as the catch pan has an inner diameter of 4 ⅛ inches, an inner depth of 5 ¾ inches, and a wall thickness of 1/32 inches. The walls and underside of the stainless steel beaker were insulated with a ¼-inch-thick sheet of silica insulation (R value of 0.3; McMaster-Carr, item no. 93435K412). A cylindrical container was chosen as the catch pan for these tests to facilitate heat transfer model development because temperature only needs to be tracked in two directions (radially from the center and vertically along the depth of the salt pool). The mitigation of heat loss to the walls of the catch pan by using insulation also simplifies the heat transfer model of this system. The mass and depth of the frozen salt in the catch pan after each spill test was measured.

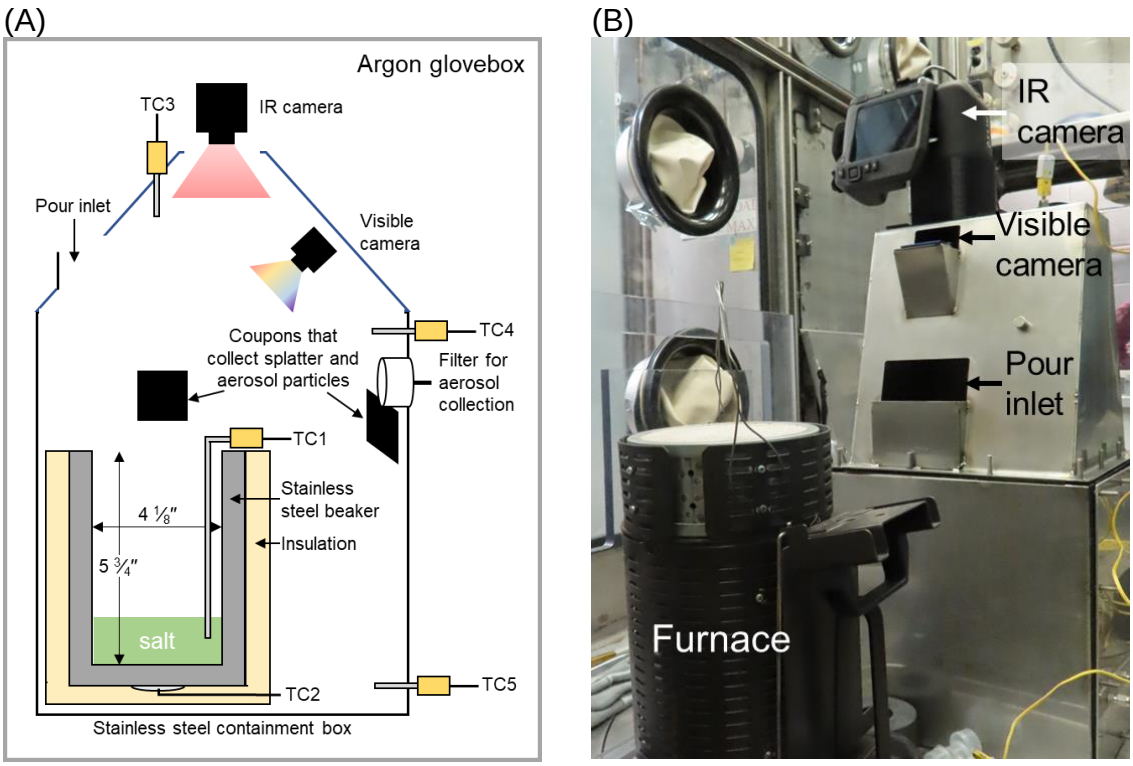

Figure 3: (A) Schematic of the setup for conducting integral effects tests on molten salt spills. (B) Photograph of the setup in the argon atmosphere glovebox.

Temperature was measured at one-second intervals using K-type thermocouples positioned at five locations within the stainless steel containment box (Figure 3A). Specifically, the thermocouples were positioned at the underside of the catch pan, in the spilled molten salt itself (near the wall of the beaker), and in three locations in the atmosphere of the containment box. The locations in the atmosphere include near the IR camera (TC3), near the aerosol collection filter (TC4), and at the bottom of the containment box (TC5; Figure 3A). A description of the thermocouples used to measure temperature throughout each test is provided in Section 4.2.4.

A PTFE filter contained within a cassette was connected to tubing that passed through a small hole in the wall of the containment box (Figure 3A) and collected aerosol particles that were present in the atmosphere during each test. The other end of the tubing was connected to a sampling pump (Buck Elite™) to pull gas from the atmosphere through the filter. The method for aerosol collection on filters, including the use of controls, is described in detail in Section 4.2.6. Nickel coupons (1 in. × 1 in.) covered with double-sided carbon tape on one side were hung near the mouth of the catch pan and beneath the aerosol collection filter to retain particles contacting the adhesive during the test for future analysis (Figure 3A).

4.2 Measurements and calculations

4.2.1 Glovebox conditions

The temperature, O_2 content, and H_2O content of the argon atmosphere glovebox was recorded before and after pouring molten salt for each test.

4.2.2 Total mass of salt poured, average pour rate, and mass of residual salt in crucible

The average pour rate of the salt into the beaker for each test was determined by dividing the total mass of salt poured from the crucible by the duration of the pour. The total mass of molten salt that was poured from the crucible was determined by measuring the mass of the crucible with residual salt after pouring and subtracting this value from the mass of the crucible that was filled with the pre-heated salt. A visible camera that was mounted on the "roof" of the stainless steel containment box recorded video of the molten salt spilling into the stainless steel beaker during each test. The duration of each pour was determined from video analysis as the time between the first and last contact of the spilled salt onto the catch pan. The camera was a GoPro HERO9 Black 5K video streaming camera that recorded video at 240 frames per second. The total mass of salt remaining in the crucible after each spill test was determined by subtracting the mass of the empty pre-weighed crucible from the mass of the crucible with residual salt.

4.2.3 Depth and mass of frozen salt accumulation in beaker

The salt that froze in the beaker during each test was removed as a single solid mass that resembled a hockey puck. The mass of the frozen salt puck was measured so that the recovered mass of salt in the beaker could be compared to the mass of salt that was poured from the crucible (as calculated in Section 4.2.2). The difference between the mass of salt recovered in the beaker and the mass of salt poured from the crucible is equal to the amount of salt that escaped the beaker as splatter, aerosols, and vapors. The average depth of the frozen salt puck in the beaker was determined by using calipers to measure the thickness of the solid salt at five locations and averaging.

4.2.4 Temperature

The furnace used to heat the salt in these experiments was a KERR Electro-Melt furnace with a 100 oz capacity. An external J-Kem 270 controller maintained the furnace at the desired target temperature. The furnace temperature was used to estimate the molten salt temperature immediately before it was poured. The initial temperature of the salt as it is being poured from the crucible was determined by using the IR camera to provide a more accurate value because the molten salt cools as it is spilled.

Thermocouples were used to measure temperature at one-second intervals using thermocouples positioned at four locations within the stainless steel containment box (Figure 3A). A *groov* Edge Programmable Industrial Controller (EPIC) from Opto 22 was used to record the temperatures from every thermocouple used in the different tests. The temperature of the underside of the catch pan was measured using K-type ceramic-insulated bare wire thermocouples with the exposed junction attached to the metal surface using thermally conductive cement. Two thermocouple probes were attached to the catch pan underside at the center. This surface temperature measurement method using thermocouple junctions attached with thermally conductive cement was previously demonstrated to provide a quick and accurate temperature response (Thomas and Jackson, 2021). A K-type grounded thermocouple probe ($\frac{1}{16}$-inch-diameter, Super OMEGACLAD™ XL sheath) was immersed in the salt near the beaker wall. The immersion depth of the thermocouple varied by test and was not recorded. Three K-type ungrounded thermocouple probes ($\frac{1}{8}$-inch-diameter, 304 stainless steel sheath) were threaded through tube fittings on the spill containment box walls and measured the temperature of the atmosphere near the IR camera, near the aerosol collection filter, and at the bottom of the containment box (Figure 3A).

A FLIR T540 IR camera with a 42° lens was used to measure the temperature of the surface of the salt that was spilled into the stainless steel beaker at one-second intervals. The highest calibration range of 300 °C to 1500 °C was used for each test, meaning that temperatures below 300 °C were not recorded. The IR camera detects infrared wavelengths within the range of 7.5 to 14 μm and has a spatial resolution of 348 × 464 pixels. The lens of the IR camera was positioned about two feet above the bottom of the stainless steel beaker. The entire beaker was in the field of view of the IR camera, and the temperature measurements had a spatial resolution of approximately 1.05 mm^2 per pixel. The temperature measurements of the eutectic FLiNaK surface were not corrected for emissivity (emissivity was assumed to be unity). The temperature measurements taken by the IR camera of the eutectic FLiNaK surface can be corrected with measured emissivity values, including emissivity measured as a function of salt temperature and physical state (i.e., liquid or solid), if they become available.

4.2.5 Elemental composition of frozen salt by using ICP-OES and ICP-MS

The concentrations of major cations (lithium, sodium, and potassium) were analyzed by using ICP-OES, and the concentrations of surrogate fission product additives (cerium, neodymium, zirconium, tellurium, molybdenum, cesium, and iodine) and possible impurities (beryllium, boron, magnesium, aluminum, silicon, calcium, chromium, iron, nickel, and copper) were analyzed by using ICP-MS. The ICP-OES measurements were made with a PerkinElmer® Optima™ 8300DV ICP optical emission spectrometer, and the ICP-MS measurements were made with a PerkinElmer® NexION® 2000 ICP mass spectrometer. Both instruments were calibrated using standards prepared from NIST-traceable solutions. The frozen salt samples were finely ground and split into two aliquots: one for metals analysis and one for iodine analysis. For metals analysis, individual salt samples were weighed, transferred to a Teflon™ Parr liner, and mixed with approximately 3 mL of deionized water, 3 mL of nitric acid (Optima™ Grade), and 1 mL of hydrochloric acid (Optima™ Grade). The Teflon™ Parr liners were then inserted into stainless steel Parr bombs and were heated overnight in a furnace at 140 °C. The salts visibly dissolved after heating. A few samples contained small amounts of a fine black material, which is suspected to be ruthenium or graphite particles from the crucible in which the salt was heated prior to testing. These solutions were then transferred to polypropylene centrifuge tubes and diluted to 25 mL with deionized water for analysis by ICP-MS.

For iodine analysis, individual salt samples were weighed and transferred to a polypropylene centrifuge tube. The salt samples in the centrifuge tubes were mixed with 2 mL of 2% boric acid and 8 mL of deionized water, and the tubes were shaken over a period of several days until the samples visibly dissolved. Some undissolved material remained in the samples for iodine analysis, but it is expected that the iodine went into solution. The samples were then further diluted to a total volume of 25 mL with deionized water and then analyzed by using ICP-MS.

For aqueous solutions, the ICP-OES technique is typically accurate to within 5% of the measured value, and the ICP-MS technique is typically accurate to within 10% of the measured value. Dissolution of salts for analyses adds to the uncertainty. The effectiveness of the method for trace iodine analysis in fluoride salts by dissolution in boric acid was verified previously (Thomas and Jackson, 2021).

4.2.6 Composition of aerosol particles by using ICP-MS

Aerosols that formed in the spill containment box during the test were collected on a 37-mm diameter PTFE filter (0.45 μm pore size) held in a cassette that was connected to a sampling pump. The pump was set to a constant flow rate of 4 L min^{-1} and was turned on approximately 30

seconds before pouring molten salt into the spill containment box to achieve a steady flow of argon gas from the glovebox through the filter. The pump was run for approximately 20 minutes after the salt was first poured into the box. The total mass of particles collected on the filter was determined by weighing the sampling cassettes before and after the tests; the efficiency of particle collection is unknown. After the test, the aerosol sampling cassette with PTFE filter was carefully removed from the spill containment box so that the collected particulates could be washed off the filter and analyzed to determine elemental composition. Control filters were used to sample the containment box atmosphere after all testing had been completed to provide a composition of the glovebox background particulates.

The ICP-MS elemental analysis of the filter samples included sodium, potassium, lithium, calcium, cerium, chromium, cesium, copper, iron, magnesium, molybdenum, neodymium, nickel, ruthenium, silicon, strontium, tellurium, zirconium, and iodine. To leach the collected particulates into solution, each filter was submerged in a PYREX® beaker containing methanol to reduce the hydrophobicity and then immediately transferred to a separate PYREX® beaker filled with a 1% boric acid solution (Ultrex Grade). The filter was leached in the 1% boric acid solution for one hour with frequent agitation of the solution, after which the filter was rinsed and removed from the solution. The contents of the beaker containing the methanol used to pre-wet the filter were added to the leachate. The combined solution was then heated on a hot plate at 70 °C for one hour to evaporate all the methanol. The solution was then diluted to 50 mL with deionized water for iodine analysis by using ICP-MS. The efficiency of the iodine recovery was tested by spiking a clean filter with a known amount of pure cesium iodide powder and using the methods described above. The recovery of iodine was 97%.

The same filters that had been leached in the boric acid solution for iodine analysis were subsequently leached in a solution of approximately 2 mL of deionized water, 2 mL of nitric acid (Optima™ Grade), and 2 mL of hydrochloric acid (Optima™ Grade) to leach any metals that were not removed by the boric acid wash. Each solution containing a filter was refluxed on a hot plate for one hour at 70 °C. Each filter was then removed from the beaker and rinsed, and the solution was diluted to 50 mL with deionized water. The diluted boric acid leach solution and the diluted nitric acid and hydrochloric acid leach solution were then combined for ICP-MS analysis to determine the total masses of the target metals that were collected on the filter.

4.2.7 Size and elemental composition of individual splatter and aerosol particles

Nickel coupons were hung near the mouth of the catch pan and just below the aerosol collection filter to collect splatter and aerosol particles for the determination of particle size and elemental composition. The coupons were covered with double-sided carbon tape to improve the adhesion of particles to the coupons. Particle size was assessed using scanning electron microscopy (SEM) and the elemental compositions of particles was determined by using energy dispersive X-ray spectroscopy (spot analysis) that was associated with SEM. To transfer coupons from the argon atmosphere glovebox to the SEM laboratory, the coupons were sealed in air-tight bags containing desiccant packets to absorb humidity and prevent water absorption by the salt particles. The coupons were quickly removed from the air-tight bags, carbon coated under vacuum, and then placed in the SEM sample chamber that was evacuated to high vacuum. The coupons were exposed to ambient air for less than two minutes during the process of transferring them from the air-tight bags into the SEM.

5 Integrated process test results

5.1 Summary of test conditions

Six tests were conducted to measure the effect of salt composition (low or high burnup) and initial salt temperature on heat transfer behavior and surrogate fission product dispersal during laboratory-scale spills of molten salt into a stainless steel catch pan. Table 7 provides a summary of the conditions of each test. The tests were conducted in the order that they are presented in Table 7. The spilled salt was collected from the stainless steel beaker and the graphite crucible after each test with the low or high burnup salt composition, crushed and combined, and then reused for the next test at a higher target initial salt temperature. The batched compositions for the low and high burnup simulated fuel salt are presented in Table 6. The levels of oxygen and moisture in the argon atmosphere remained below 10 ppm O_2 and 1 ppm H_2O during each test.

Table 7: Summary of integrated process test conditions

Salt Composition	Target initial salt temp. (°C)[a]	Max salt temp. (°C)[b]	Mass salt poured (g)	Mass salt recovered (beaker, g)[c]	Mass salt recovered (crucible, g)[c]	Avg. salt depth (mm)[d]	Avg. pour rate (g s^{-1})
Low burnup	650	592	272.4	272.2	47.8	15.4 ± 2.5	48.6
Low burnup	750	685	261.4	261.2	53.6	14.9 ± 1.7	45.9
Low burnup	850	786	287.6	287.4	24.0	16.3 ± 1.7	59.9
High burnup	650	538	310.5	309.3	9.5	17.1 ± 0.4	64.7
High burnup	750	663	262.6	262.5	50.1	14.1 ± 0.9	54.7
High burnup	850	779	295.7	295.5	13.9	16.8 ± 0.6	46.9

[a] The actual initial salt temperature may be lower than the target temperature due to cooling while spilling.
[b] The maximum temperature of the salt measured by the IR camera (assumed salt emissivity of 1) provided an estimate of the actual salt temperature as it was poured.
[c] The mass of the frozen salt recovered from the stainless steel beaker or crucible after each spill test.
[d] Reported values are average and one standard deviation of five measurements.

5.2 Visible video of molten salt spill behavior

Slow motion video of the salt spilling into the beaker was recorded for each test by using a visible camera at a rate 0.05 times lower than real-time. The main purpose of the visible camera was to enable the observation of the spill behavior and to use the footage to determine the spill duration so that the average spill rate could be calculated. The spatial and temporal resolution of the camera were not high enough to capture details on the splashing behavior or formation of bubbles at the molten salt surface. These processes could be observed by using a high-speed camera in future tests. Figure 4 provides still frames taken at one and two seconds after the salt first touched the beaker floor for the test conducted with high burnup FLiNaK at an initial salt temperature of approximately 850 °C. The salt appears as a pink-red color in Figure 4 due to the incandescence of the hot salt. A thermocouple immersed in the salt can be seen at the lower right side of the beaker. The salt was spilled into the beaker as a continuous stream at an average rate ranging from 45 to 65 g s^{-1} (Table 7). The duration of the spill for each test was approximately five seconds. The force of salt impact onto the beaker floor can be described as relatively gentle and was governed by the inertia of the salt leaving the crucible and gravity; the salt fell a distance of approximately 15 inches from the crucible to the beaker floor.

Bubbles of entrained gas from the atmosphere may have formed in the molten salt pool as salt spilled into the beaker; however, the occurrence of this process cannot be confirmed due to the insufficient resolution of the visible camera. The splashing behavior of the low and high burnup

FLiNaK was similar to the splashing behavior observed during previous tests with pure FLiNaK (Thomas and Jackson, 2021) and eutectic NaCl-UCl_3 (Thomas and Jackson, 2022). The salt broke up into smaller particles upon impact with the beaker floor, and the particles adhered to the walls of the beaker. The adhered splatter eventually fell off the beaker walls during the test due to gravity or after the test when the beaker was moved to recover the spilled frozen salt. Slow motion visible video of the molten low and high burnup FLiNaK spilling into the beaker for each test is available from the lead author in the data package associated with this report.

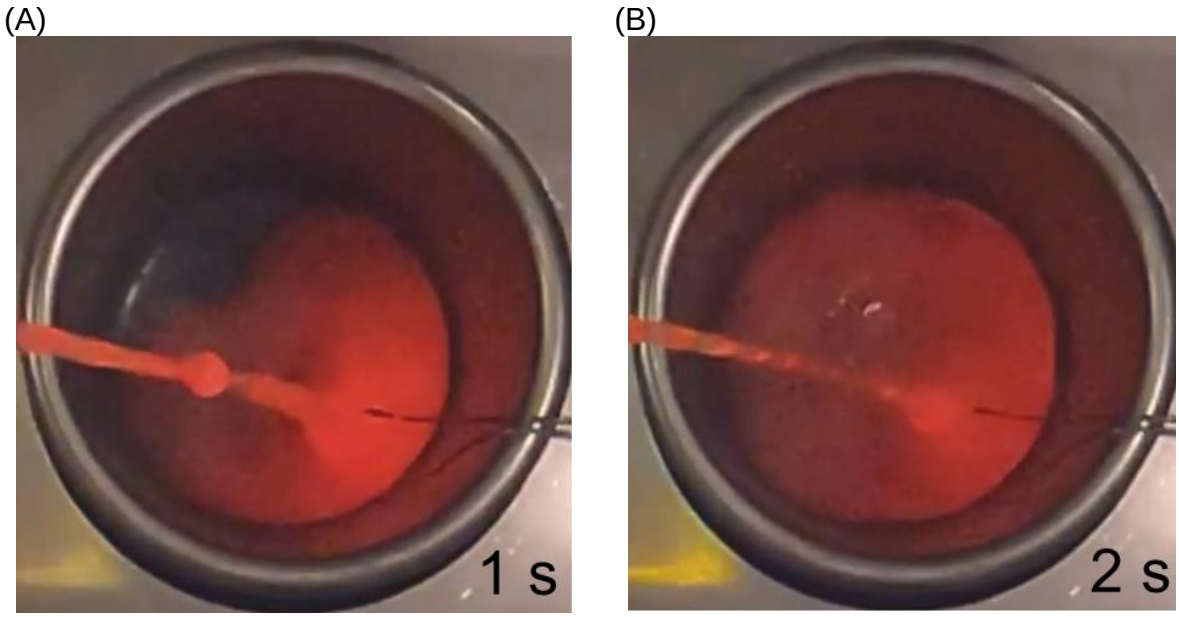

Figure 4: Still video frames of high burnup salt at a target initial temperature of 850 °C pouring into the beaker (A) 1 second and (B) 2 seconds after the salt first touched the beaker floor.

5.3 Salt surface temperature measurements by using an infrared camera

Still frames taken by the IR camera of the low and high burnup surrogate fuel salt surface temperature in the stainless steel beaker after pouring salt at initial temperatures of 650 °C, 750 °C, and 850 °C are presented in Figure 5, Figure 6, and Figure 7, respectively. The thermocouple immersed in the salt obstructed the view in some of the frames, and black circles mark the interface of the salt and inner diameter of the beaker (Figure 5, Figure 6, and Figure 7).

In general, the salt surface temperature measured by the IR camera appears more spatially uniform for the low burnup surrogate fuel salt composition than for the high burnup composition (Figure 5, Figure 6, and Figure 7). A non-uniform temperature distribution over the salt surface when measured by an IR camera could be due to compositional heterogeneity that creates a non-uniform emissivity over the salt surface. Non-uniform emissivity over the salt surface would affect the apparent temperature that is measured by the IR camera and make the temperature appear non-uniform when the actual temperature is uniform. Insoluble salt components (e.g., ruthenium metal) and graphite particles present at the salt surface likely contributed to the compositional heterogeneity at the salt surface. Figure 8 shows a layer of graphite covering the top surface of a piece of frozen salt collected after the test with high burnup FLiNaK that was spilled at an initial temperature of 850 °C. It is also possible that the surface temperature measured by the IR camera appears non-unform because the surface temperature is truly non-uniform.

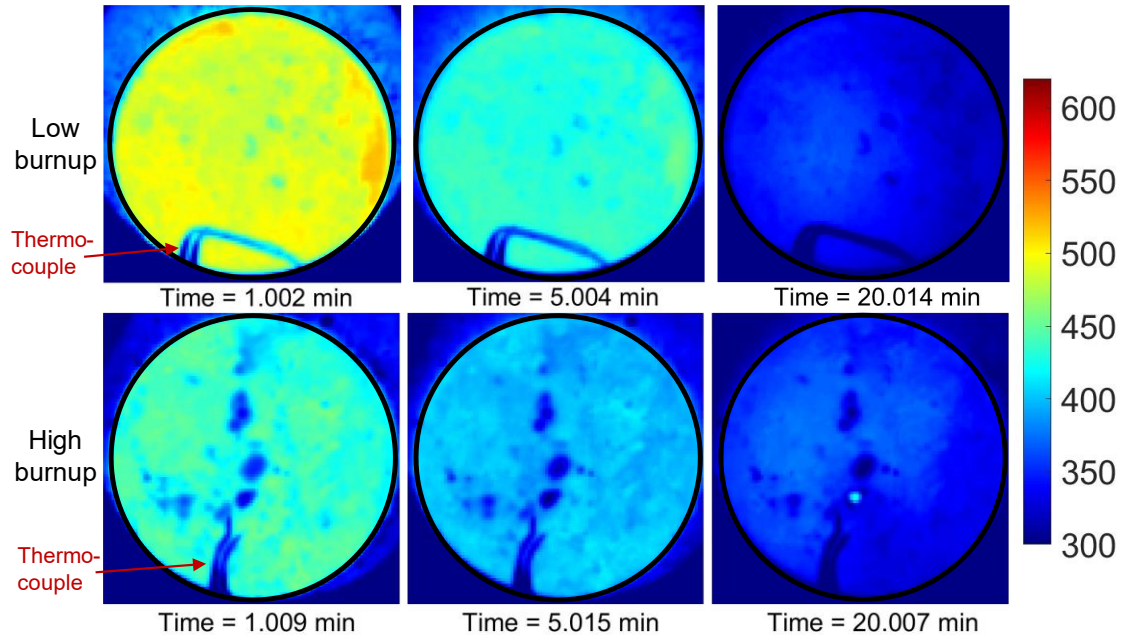

Figure 5: The surface temperatures (°C) of the low and high burnup surrogate fuel salts in the stainless steel beakers after pouring at an initial temperature of approximately 650 °C over time. The indicated time is the time elapsed after pouring the molten salt into the beaker. A thermocouple and thermocouple holder near the bottom of the frame obstructed the view of the salt surface.

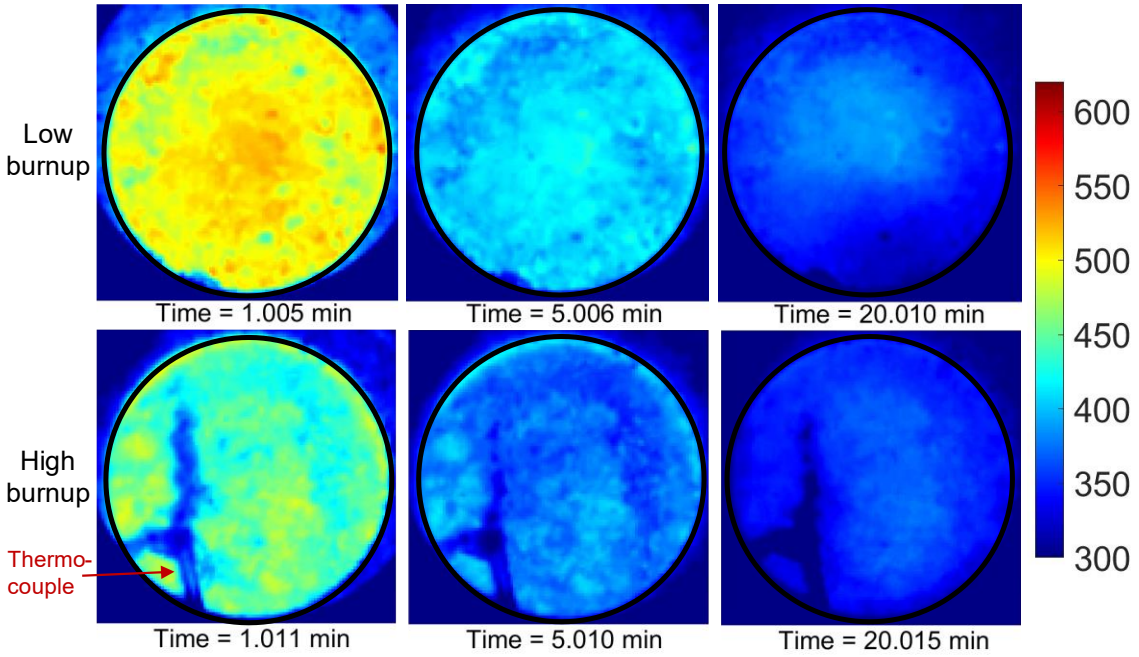

Figure 6: The surface temperatures (°C) of the low and high burnup surrogate fuel salts in the stainless steel beakers after pouring at an initial temperature of approximately 750 °C over time. The indicated time is the time elapsed after pouring the molten salt into the beaker. A thermocouple and thermocouple holder near the bottom of the frame obstructed the view of the salt surface.

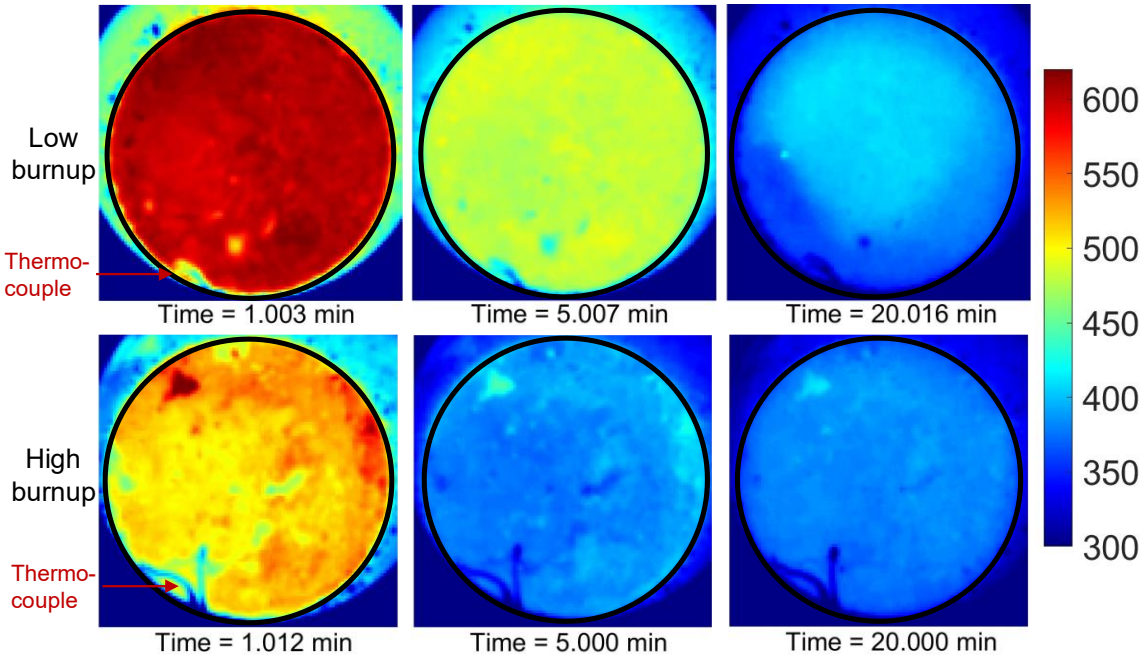

Figure 7: The surface temperatures (°C) of the low and high burnup surrogate fuel salts in the stainless steel beakers after pouring at an initial temperature of approximately 850 °C over time. The indicated time is the time elapsed after pouring the molten salt into the beaker. A thermocouple and thermocouple holder near the bottom of the frame obstructed the view of the salt surface.

Figure 8: Cross-section of frozen salt that shows graphite particles at salt surface.

The salt at the surface does not cool markedly faster at the beaker walls (Figure 5, Figure 6, and Figure 7), as had been observed in previous tests that used stainless steel beakers without insulation covering the outer walls (Thomas and Jackson, 2022). In addition, the salt surface temperature of the high burnup salt composition appears to be lower than that of the low burnup salt composition when comparing the frames taken for spills conducted at the same initial salt temperature and at the same time after the spill (Figure 5, Figure 6, and Figure 7). This is clear in the plot of the apparent salt surface temperature measured by the IR camera at the center of the beaker over time for each test (Figure 9). The lower apparent surface temperature measured by the IR camera (i.e., temperature measurement not corrected for emissivity) for the high burnup salt when compared to the low burnup salt under the same spill conditions could be due to the high burnup salt composition having a lower emissivity than the low burnup salt composition. A lower apparent salt surface temperature for the high burnup salt composition could also be due to

the two salt compositions having different thermal properties or a combination of having different thermal properties and emissivities. Recent analyses suggest that both salt compositions have similar thermal profiles, heat capacities, and thermal diffusivities (Gardner and Rose, 2023). The emissivities of both FLiNaK-based salt compositions have not yet been measured.

The salts that were spilled at higher initial temperatures take longer to cool than those spilled at lower initial temperatures (Figure 5, Figure 6, and Figure 7). This is apparent in Figure 9. The time after the spill at which the salt surface temperature reaches approximately 300 °C, except for the high burnup salt composition at 650 °C, increases with increasing initial salt temperature (Figure 9). The test conducted with the high burnup salt composition at an initial temperature of 650 °C had a higher spill mass than any other test (Table 7), which explains the longer time required to reach a surface temperature of 300 °C. The apparent salt surface temperature measured by the IR camera plateaus at a temperature between 370 °C and 430 °C, depending on the test, due to the phase transition from liquid to solid (Figure 9). The emissivity of each salt composition can be estimated using the known melting temperature, the apparent melting temperature measured by the IR camera, and the equation for calculating the emissivity of a non-transparent object (Thomas and Jackson, 2021, 2022). The melting behaviors of the low and high burnup salt compositions measured by using differential scanning calorimetry (DSC) are similar (Gardner and Rose, 2023). The liquidus and solidus temperatures from DSC thermal analyses of both FLiNaK compositions are approximately 470 °C and 445 °C, respectively (Gardner and Rose, 2023). The fact that the melting temperatures of the two salt compositions are the same based on measurements using DSC but different based on IR camera measurements (Figure 9) indicates that the emissivity of the high burnup salt composition is lower than that of the low burnup salt composition. There is some fluctuation in the apparent salt surface temperature measured by the IR camera near the melting temperature for each test, which is more pronounced in measurements of the high burnup salt composition (Figure 9). These temperature fluctuations can be attributed to supercooling and changes in the salt emissivity as the salt changes phase from liquid to solid.

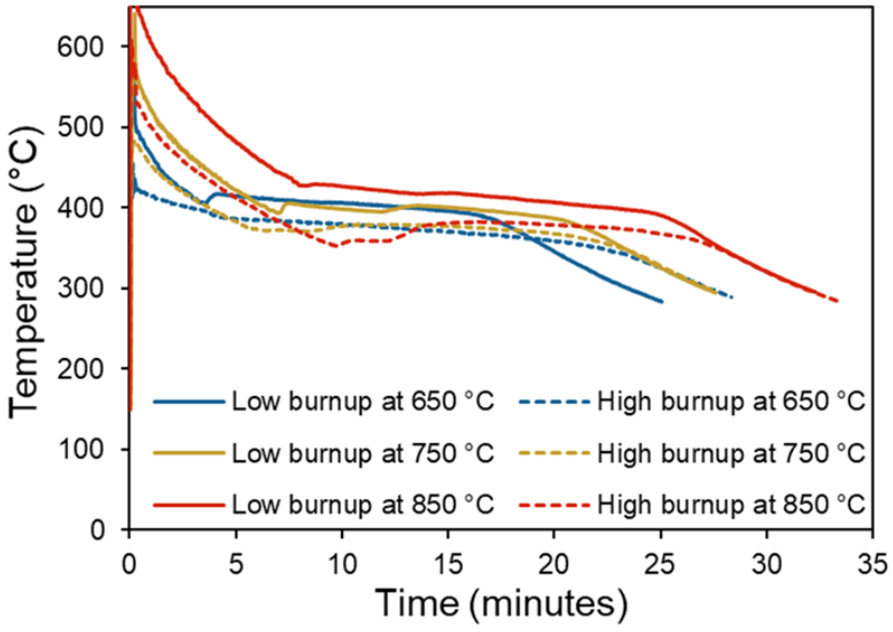

Figure 9: The apparent salt surface temperature at the center of the beaker as measured by the IR camera plotted as a function of time for each test. The reported temperatures have not been corrected for the emissivity of each salt composition.

The IR video frames that report the salt surface temperatures of the low and high burnup simulated fuel salt for the six tests that were conducted were converted to .csv files and are available in the data package associated with this report. The temperatures of the center pixel measured by the IR camera for each test plotted in Figure 9 are also available in spreadsheet form in the data package associated with this report.

5.4 Temperature measurements by salt-immersed thermocouple

The temperatures measured by a K-type grounded thermocouple (1/16″-diameter OMEGACLAD™ XL sheath) that was immersed in the salt near the salt surface are plotted over time for each test in Figure 10. This salt-immersed thermocouple was slightly bowed and its exact depth in the salt is unknown and varied between tests. Temperature measurements for the test conducted with the low burnup composition at an initial temperature of 650 °C were not made because the thermocouple was not immersed in the salt. The approximate thermocouple position relative to the beaker wall is shown for each test in Figure 5, Figure 6, and Figure 7.

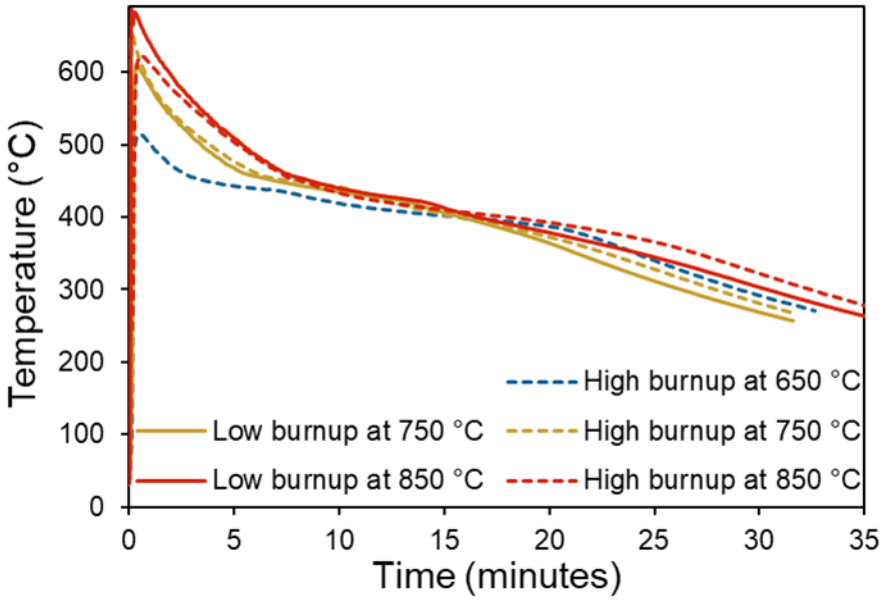

Figure 10: The salt temperature as measured by the salt-immersed thermocouple plotted as a function of time for each test. The results from the test conducted with the low burnup composition at an initial temperature of 650 °C are not shown.

All temperature measurements exhibit a slight plateau near the melting point of pure FLiNaK (approximately 450 °C) but do not completely level off. This is likely due to the thermocouple junction being only slightly below the salt surface, which cools faster than the bulk salt, and the fact that salt-immersed thermocouples are known to be heat sinks. The salt-immersed thermocouples employed in these tests were expected to be less-effective heat sinks than the thermocouples employed previously (Thomas and Jackson, 2022) due to the smaller sheath diameter and the use of ceramic insulation around the exposed sheath. However, these changes likely did not eliminate the heat sink effect.

The data files of the temperature measurements by the salt-immersed thermocouple are available in the data package associated with this report.

5.5 Temperature of the underside of the stainless steel beaker

The temperature of the underside of the stainless steel beaker was measured over the duration of each test at one-second intervals using bare wire K-type thermocouples with the junctions fixed to the surface with thermally conductive cement. The averages of replicate measurements from two adjacent thermocouples positioned at the center of the beaker underside are plotted in Figure 11. The data logger failed to record the full temperature measurement for the low burnup composition at an initial temperature of 650 °C, and only results for the first six minutes are shown in Figure 11.

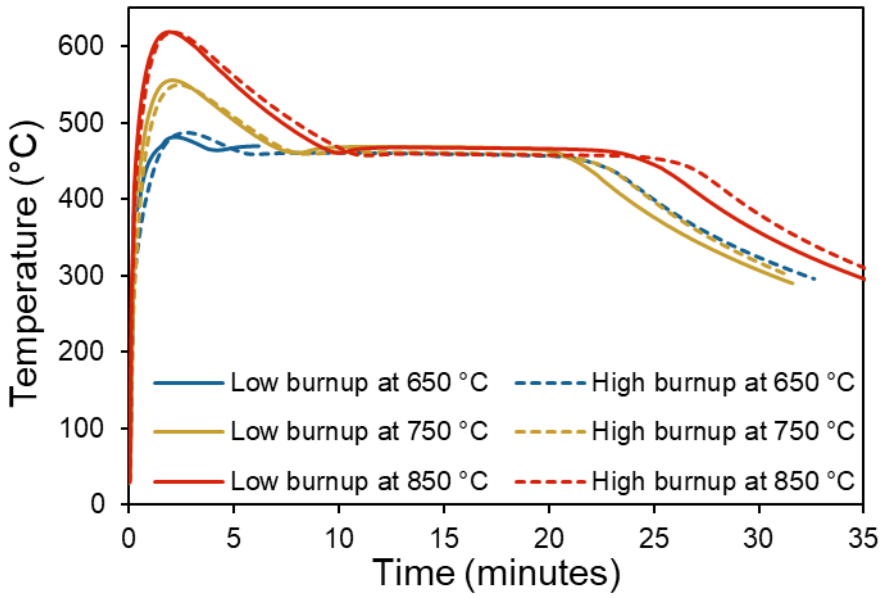

Figure 11: (A) The beaker underside temperature plotted as a function of time as measured by thermocouples attached to the surface for all tests. The data logger failed to record the full temperature measurement for the low burnup composition at an initial temperature of 650 °C.

The maximum temperatures measured at the beaker underside are very similar for the tests conducted with the low and high burnup salt compositions that were spilled at the same initial temperature (Figure 11). The maximum temperatures reached at the beaker underside increase with the initial temperature of the spilled salt (Figure 11). In addition, the beaker underside temperature plateaus at the melting temperature of the salt. Most of the heat loss from the spilled salt should occur from the salt surface because the beaker underside and walls are insulated. Minimal heat loss from the base of the beaker would lead to the beaker underside temperature reaching the same temperature as the salt in direct contact with the base of the beaker, which explains the temperature plateau at the salt melting temperature for each temperature curve shown in Figure 11. In fact, the melting temperature of the salt can be estimated from the plateau in the cooling curve in Figure 11. The mode of the measured beaker underside temperatures obtained from the cooling curves is used to estimate the melting temperature of the salts and is presented for each test in Table 8. The estimated melting temperatures in Table 8 all fall within the liquidus and solidus temperatures measured by using DSC for both salt compositions (Gardner and Rose, 2023). The data files of the beaker underside temperature measurements are available in the data package associated with this report.

Table 8: The mode of the measured beaker underside temperatures for each test

Low burnup at 650 °C	Low burnup at 750 °C	Low burnup at 850 °C	High burnup at 650 °C	High burnup at 750 °C	High burnup at 850 °C
not measured	468.2	467.4	460.5	461.2	457.2

5.6 Temperature of the atmosphere of the containment box

The temperature of the atmosphere of the stainless steel containment box was measured over the duration of each test at one-second intervals using K-type ungrounded thermocouples with ⅛-inch-diameter and 304 stainless steel sheaths. The atmosphere temperatures measured near the IR and visible cameras, near the aerosol collection filter, and near the floor of the containment box are presented in Figure 12, Figure 13, and Figure 14, respectively. The approximate locations of the thermocouples that measured the temperature of the atmosphere (i.e., TC3, TC4, and TC5) are shown in Figure 3A. Some temperatures were not recorded over the entire test duration, as indicated in Figure 12, Figure 13, and Figure 14.

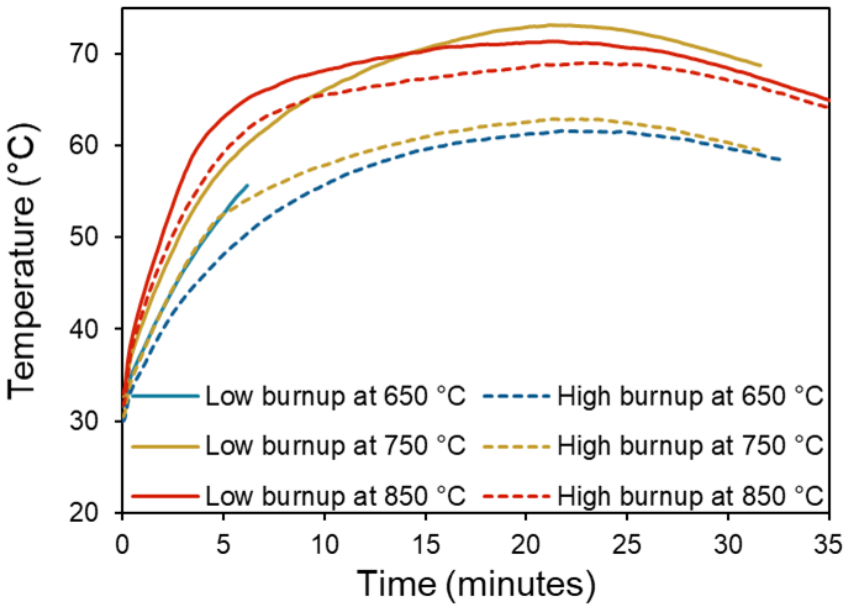

Figure 12: The temperature of the atmosphere in the stainless steel containment box near the IR and visible cameras measured by thermocouple TC3. The temperature did not record over the entire test duration for the low burnup test at 650 °C.

The maximum atmosphere temperature measured by each thermocouple for each test is presented in Table 9. The data logger failed to record all thermocouple measurements beyond the first six minutes of the test conducted with the low burnup salt composition at an initial temperature of 650 °C; a maximum temperature is not provided for that test in Table 9. Thermocouple TC3 was positioned approximately six inches below the ceiling of the containment box and recorded the highest atmosphere temperatures. The visible camera was removed from its position on the roof of the containment box after recording was completed for the test using the low burnup composition at 850 °C and for all tests using the high burnup composition to minimize its exposure to the heat. The removal of the visible camera, and increased ventilation in the containment box in

consequence, promoted cooling in the containment box atmosphere. The maximum recorded temperature near the aerosol collection filter was between 44 °C and 63 °C for all tests (Table 9). The temperature near the containment box floor was much lower than the temperature near the containment box ceiling (Table 9). The data files of the atmosphere temperature measurements are available in the data package associated with this report.

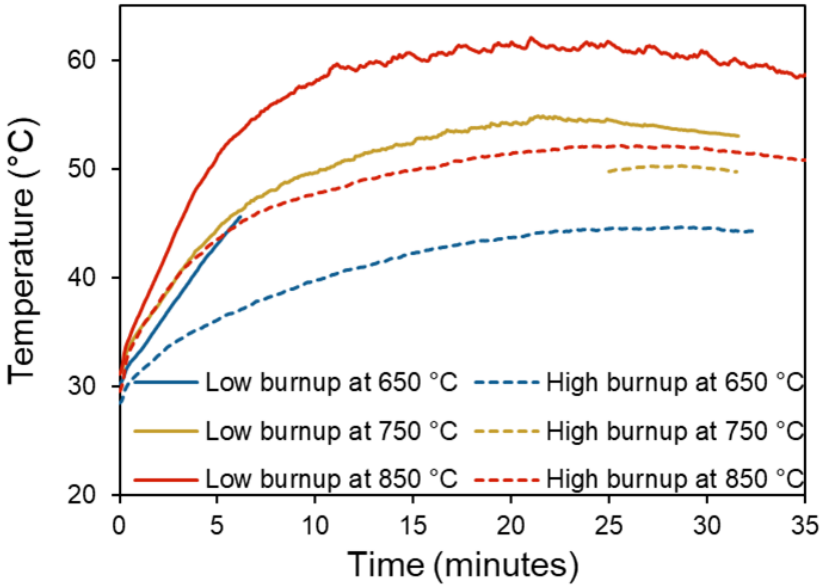

Figure 13: The temperature of the atmosphere in the stainless steel containment box near the aerosol collection filter measured by thermocouple TC4. The temperature did not record over the entire test duration for the low burnup test at 650 °C and the high burnup test at 750 °C.

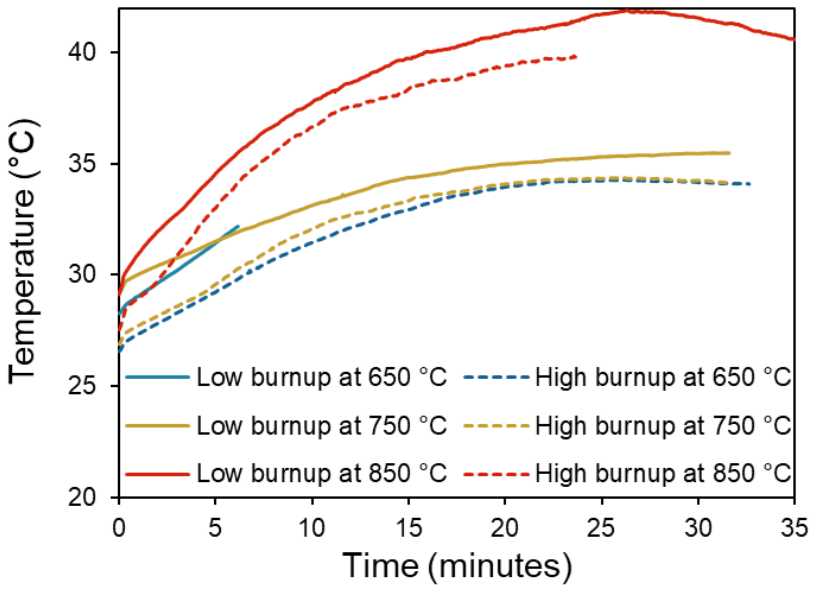

Figure 14: The temperature of the atmosphere in the stainless steel containment box near the floor measured by thermocouple TC5. The temperature did not record over the entire test duration for the low burnup test at 650 °C and the high burnup test at 850 °C.

Table 9: The maximum measured atmosphere temperature (°C) by three thermocouples for each test

Thermocouple	Low burnup at 650 °C	Low burnup at 750 °C	Low burnup at 850 °C	High burnup at 650 °C	High burnup at 750 °C	High burnup at 850 °C
TC3	not determined	73.2	71.4	61.6	62.9	69.0
TC4	not determined	54.9	62.1	44.7	50.3	52.2
TC5	not determined	35.5	41.9	34.3	34.4	39.8

5.7 Bulk salt composition by ICP-OES and ICP-MS

Frozen salt samples were collected from the stainless steel beaker into which the molten salt was poured and from the graphite crucible from which the molten salt was poured for elemental composition analysis. A fraction of salt remained in the crucible after each spill test and samples of frozen salt were collected from the crucible so that a mass balance could be performed to measure the recovery of surrogate fission products. The entire amount of frozen salt collected from both sampling locations was separately ground into a powder using a stainless steel mortar and pestle to homogenize the frozen salt. Three samples of each powder were taken for composition analysis. The concentrations of the major cations lithium, sodium, and potassium were determined by using ICP-OES and the concentrations of all other elements were determined by using ICP-MS according to the methods described in Section 4.2.5. Table 10 provides the concentrations of major salt components (LiF, NaF, and KF) and impurities (chromium and nickel) and Table 11 provides the concentrations of surrogate fission products in the same frozen salt samples taken from the stainless steel beaker and graphite crucible. The concentrations presented in Table 10 and Table 11 are averages from analyses of triplicate samples taken from the specified location.

The concentrations of LiF, NaF, and KF measured in most of the frozen salt samples that were collected from the beaker after each test are consistent with the batched compositions within the expected error of the measurement (i.e., 5%; Table 10). The KF concentrations measured in the frozen salt collected from the beakers for the three tests conducted with the low burnup FLiNaK differ most from the batched composition and have the highest standard deviations among the measured major components. The frozen salt collected from the beaker for these tests likely required further compositional homogenization and a larger sample size would likely yield an average measured KF concentration that is closer to the batched concentration. The concentrations of LiF, NaF, and KF measured in the samples taken from the crucible differ from the batched compositions more than those measured in the beaker. This is likely due to a greater presence of graphite particles and other non-FLiNaK components (e.g., surrogate fission product precipitates) in the salt remaining in the crucible. This would yield concentrations of LiF, NaF, and KF in the salt remaining in the crucible that differ from the batched concentrations. The main impurities detected in the frozen salt samples taken from the crucible and beaker were chromium and nickel (Table 10). The chromium and nickel could have been introduced into the salt by corrosion of the stainless steel beaker. It is notable that the chromium and nickel concentrations do not appear to increase in measurements made at higher temperatures because the salt recovered from the beaker and crucible from tests conducted at 650 °C was reused to conduct tests at 750 °C and then tests at 850 °C; the total exposure time of molten salt to the stainless steel beaker increased as the salt was reused in each subsequent test. The concentrations of

potential impurities beryllium, boron, magnesium, aluminum, silicon, calcium, iron, and copper were all below the detection limit of the ICP-MS.

Table 10: Concentration of major components and impurities in frozen salt samples[a,b]

Composition	Target initial temp. (°C)	Sample location	LiF (mol %)	NaF (mol %)	KF (mol %)	Cr (ppm)	Ni (ppm)
Low burnup	650	Crucible	45.6 ± 2.6	11.9 ± 0.8	44.5 ± 5.0	11.2 ± 4.5	307 ± 220
		Beaker	45.9 ± 3.6	12.0 ± 1.0	44.8 ± 5.8	16.0 ± 1.3	106 ± 98
Low burnup	750	Crucible	42.9 ± 0.1	11.1 ± 0.03	40.3 ± 0.2	11.2 ± 3.1	192 ± 42
		Beaker	46.0 ± 3.6	12.0 ± 1.2	46.3 ± 8.5	17.5 ± 0.9	62.0 ± 64
Low burnup	850	Crucible	43.2 ± 0.4	11.2 ± 0.1	40.7 ± 0.3	20.1 ± 8.6	335 ± 170
		Beaker	44.2 ± 3.0	11.5 ± 0.8	42.5 ± 4.2	20.8 ± 4.9	13.2 ± 7.6
	Low burnup batched composition (mol %)		46.3	11.5	41.8	–	–
High burnup	650	Crucible	44.9 ± 0.2	11.2 ± 0.04	40.6 ± 0.3	14.1 ± 0.2	639 ± 260
		Beaker	45.3 ± 1.7	11.4 ± 0.5	42.3 ± 2.9	17.3 ± 0.8	69.0 ± 48
High burnup	750	Crucible	43.9 ± 1.2	11.0 ± 0.3	40.2 ± 0.8	22.4 ± 10	190 ± 14
		Beaker	44.6 ± 0.4	11.3 ± 0.1	41.0 ± 0.4	18.3 ± 5.8	64.0 ± 32
High burnup	850	Crucible	39.0 ± 1.6	9.8 ± 0.4	35.5 ± 1.4	12.7 ± 4.6	1860 ± 410
		Beaker	43.5 ± 0.4	11.0 ± 0.1	40.0 ± 0.3	15.4 ± 2.4	8.0 ± 2.0
	High burnup batched composition (mol %)		45.7	11.3	41.2	–	–

[a] Mol % LiF, NaF, and KF was calculated assuming all measured Li, Na, and K was present as a fluoride species and using a molecular weight for the low and high burnup salt of 41.685 g mol^{-1} and 43.247 g mol^{-1}, respectively, that was calculated from the batched composition.
[b] The reported values are the mean ± one standard deviation.

Knowing the concentration of each surrogate fission product that remained in the crucible and was poured into the stainless steel beaker provides insight into whether the surrogate fission product additives were dissolved in the salt before the salt was poured. The concentrations of cerium, neodymium, zirconium, cesium, and iodine measured in the frozen salt samples collected from the crucible and the beaker for tests conducted using the low burnup salt are consistent with the batched compositions (Table 11). This indicates that these elements were completely dissolved in the salt before it was poured. The concentrations of zirconium, cesium, and iodine measured in the frozen salt samples collected from the crucible and the beaker for tests conducted using the high burnup salt are also consistent with the batched compositions (Table 11). The salt samples taken from the crucible had higher concentrations of cerium and neodymium than those taken from the beaker for tests conducted with high burnup salt, possibly because the amounts of added CeF_3 and NdF_3 exceeded their solubility limits in FLiNaK. Precipitates containing neodymium and cerium that formed in the salt could have settled to the bottom of the crucible and avoided being poured into the beaker.

The concentrations of tellurium and molybdenum in the salt samples collected from the crucible and beaker for all tests conducted differ, sometimes considerably, from the batched compositions. The large differences in tellurium and molybdenum concentration measured in the salt collected

from the crucible and beaker for the same test indicate that these elements were likely not completely dissolved in the salt before it was poured. The tellurium concentrations measured in salt samples from tests conducted using the low burnup salt composition are the closest to the batched concentration among all molybdenum and tellurium concentration results, suggesting that some tellurium is soluble in FLiNaK. For most tests, the concentrations of tellurium and molybdenum are much higher in the salt samples taken from the crucible than in those taken from the beaker. This observation can be attributed to these elements being present as separate phases from the liquid salt mixture, likely as solids rather than immiscible liquids due to the high melting temperatures of molybdenum metal and Na_2Te. The separated molybdenum and tellurium phases partitioned to the fraction of the salt that remained in the crucible after pouring. The solubilities of molybdenum metal and Na_2Te in molten FLiNaK are unknown.

Strontium was not detected in any frozen salt sample collected for the tests with the low burnup salt composition and detected at a concentration that was much lower than the batched concentration in salt samples from the high burnup salt composition (Table 11). It is unknown why this occurred. It is unlikely that the SrF_2 completely vaporized in the furnace while the mixtures of FLiNaK and surrogate fission product powders were being heated to the target temperature because the pure species vapor pressure of SrF_2 is much lower than those of other pure species that were detected in the salt (i.e., Na_2Te and CsI). Ruthenium was not detected using the ICP-MS technique described in Section 4.2.5. This indicates that ruthenium remained metallic in the salt and was not dissolved in the acidic aqueous solution that was prepared for ICP-MS analysis.

Knowing the total amount of each surrogate fission product additive that was spilled into the stainless steel beaker facilitates an assessment of the dispersal behavior of these elements as components of splatter and aerosol particles. A mass balance was performed using the measured concentrations of surrogate fission products in frozen salt samples taken from the crucible and from the beaker. These concentrations were multiplied by the mass of frozen salt that was measured in each location after each test to determine the total amounts of that element present in the salt poured into the beaker and remaining in the crucible. The mass of frozen salt measured in the beaker and in the crucible after each test is provided in Table 7. The total masses of cerium, neodymium, zirconium, tellurium, molybdenum, cesium, and iodine present in the portion of salt that remained in the crucible and the portion that was poured into the beaker are compared to the total batched mass of each element for each test in Figure 15, Figure 16, Figure 17, Figure 18, Figure 19, Figure 20, and Figure 21, respectively.

The total recovered mass of cerium, neodymium, zirconium, cesium, and iodine after testing (sum of the masses measured in crucible and beaker) agrees well with the total batched mass for the tests conducted with the low burnup salt (Figure 15A, Figure 16A, Figure 17A, Figure 20A, and Figure 21A). Likewise, the total recovered mass of zirconium, cesium, and iodine after testing agrees well with the total batched mass for the tests conducted with the high burnup salt (Figure 17B, Figure 20B, and Figure 21B). The near complete recovery of these elements after testing confirms their uniform distribution in the salt with minimal loss to vaporization during heating in the furnace and during testing. In addition, near complete recovery after testing strongly indicates that the CeF_3, NdF_3, ZrF_4, CsF, and CsI were completely dissolved in the low burnup salt composition and that ZrF_4, CsF, and CsI were completely dissolved in the high burnup salt composition.

Table 11: Concentration of surrogate fission product elements in frozen salt samples (wt %)[a,b,c.]

Composition, target initial temp. (°C)	Sample location	Ce	Nd	Sr	Zr	Te	Mo	Cs	I
Low burnup 650	Crucible	0.17 ± 0.02	0.20 ± 0.01	n.d.	0.12 ± 0.02	0.036 ± 0.02	0.39 ± 0.3	0.19 ± 0.02	0.017 ± 0.001
	Beaker	0.17 ± 0.009	0.19 ± 0.007	n.d.	0.11 ± 0.009	0.014 ± 0.004	0.028 ± 0.02	0.18 ± 0.02	0.018 ± 0.001
Low burnup 750	Crucible	0.16 ± 0.004	0.17 ± 0.003	n.d.	0.10 ± 0.001	0.017 ± 0.003	0.13 ± 0.02	0.17 ± 0.006	0.016 ± 0.001
	Beaker	0.17 ± 0.006	0.18 ± 0.02	n.d.	0.11 ± 0.006	0.013 ± 0.001	0.059 ± 0.03	0.19 ± 0.02	0.016 ± 0.001
Low burnup 850	Crucible	0.17 ± 0.004	0.19 ± 0.003	n.d.	0.11 ± 0.005	0.016 ± 0.002	0.45 ± 0.2	0.17 ± 0.003	0.017 ± 0.001
	Beaker	0.16 ± 0.009	0.18 ± 0.03	n.d.	0.11 ± 0.01	0.013 ± 0.001	0.035 ± 0.01	0.18 ± 0.03	0.017 ± 0.002
Low burnup batched composition (wt %)		0.16	0.18	0.10	0.11	0.019	0.11	0.18	0.018
High burnup 650	Crucible	0.81 ± 0.03	0.86 ± 0.02	$3.5 \cdot 10^{-4} \pm 4 \cdot 10^{-5}$	0.50 ± 0.02	0.12 ± 0.02	1.0 ± 0.51	0.83 ± 0.01	0.066 ± 0.002
	Beaker	0.47 ± 0.06	0.58 ± 0.07	$4.0 \cdot 10^{-4} \pm 8 \cdot 10^{-5}$	0.51 ± 0.05	0.04 ± 0.02	0.15 ± 0.02	0.79 ± 0.1	0.067 ± 0.001
High burnup 750	Crucible	0.58 ± 0.3	0.70 ± 0.2	$4.4 \cdot 10^{-4} \pm 6 \cdot 10^{-5}$	0.48 ± 0.01	0.10 ± 0.01	1.0 ± 0.4	0.83 ± 0.01	0.064 ± 0.001
	Beaker	0.54 ± 0.3	0.62 ± 0.2	$5.3 \cdot 10^{-4} \pm 1 \cdot 10^{-4}$	0.48 ± 0.03	0.04 ± 0.006	0.28 ± 0.04	0.81 ± 0.04	0.068 ± 0.002
High burnup 850	Crucible	0.69 ± 0.02	0.76 ± 0.03	$1.8 \cdot 10^{-4} \pm 9 \cdot 10^{-5}$	0.46 ± 0.03	0.47 ± 0.03	4.7 ± 0.5	0.70 ± 0.02	0.057 ± 0.002
	Beaker	0.41 ± 0.2	0.53 ± 0.1	$3.7 \cdot 10^{-4} \pm 9 \cdot 10^{-6}$	0.44 ± 0.02	0.03 ± 0.001	0.086 ± 0.02	0.79 ± 0.04	0.069 ± 0.002
High burnup batched composition (wt %)		0.81	0.83	0.51	0.52	0.073	0.54	0.84	0.073

[a] The reported values are the mean ± one standard deviation.
[b] "n.d." means not detected.
[c] The concentration of ruthenium in salt samples was not able to be measured using ICP-MS.

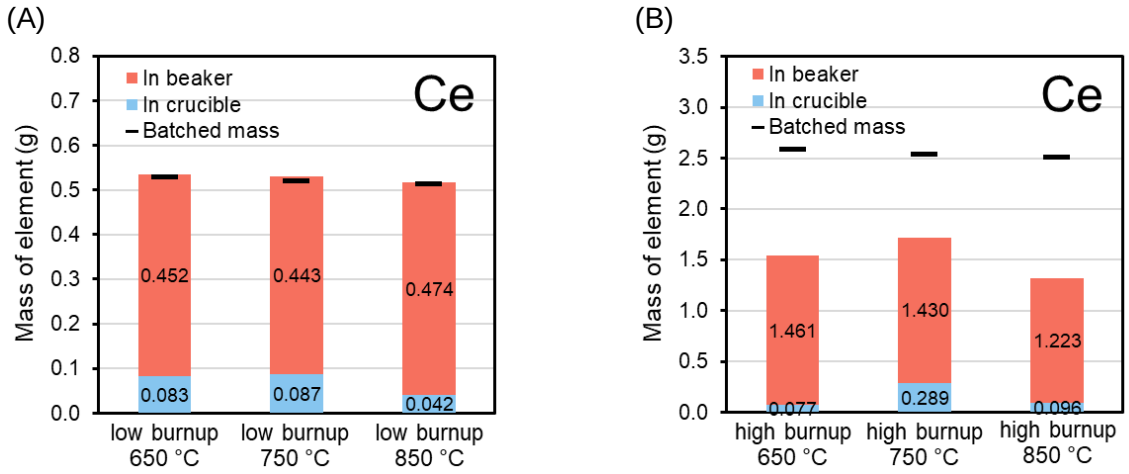

Figure 15: The total measured mass of cerium in the crucible and in the beaker compared to the total batched mass for tests conducted using the (A) low and (B) high burnup salt.

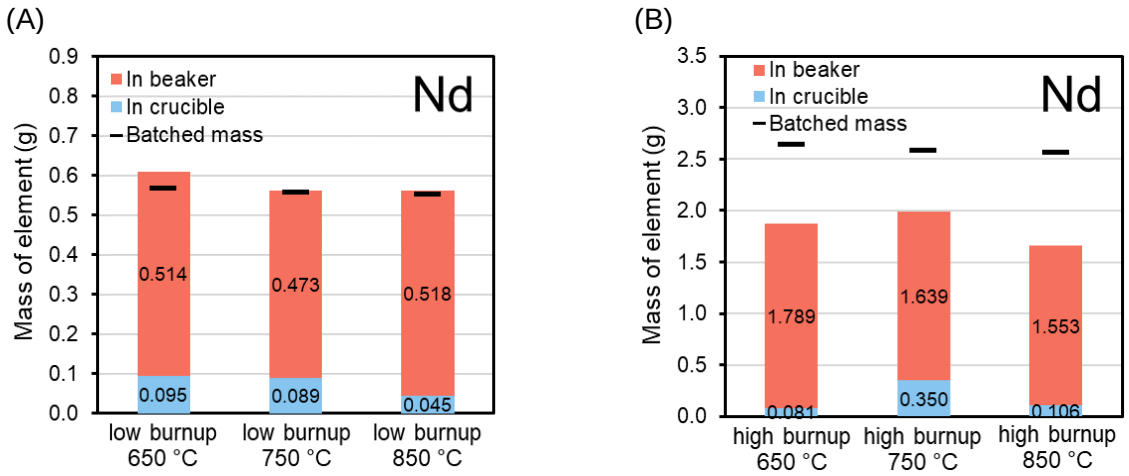

Figure 16: The total measured mass of neodymium in the crucible and in the beaker compared to the total batched mass for tests conducted using the (A) low and (B) high burnup salt.

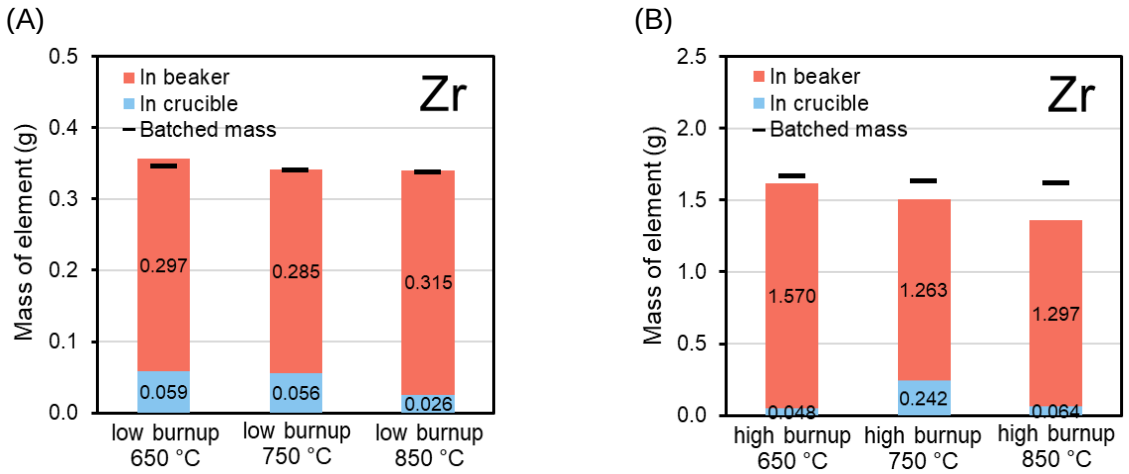

Figure 17: The total measured mass of zirconium in the crucible and in the beaker compared to the total batched mass for tests conducted using the (A) low and (B) high burnup salt.

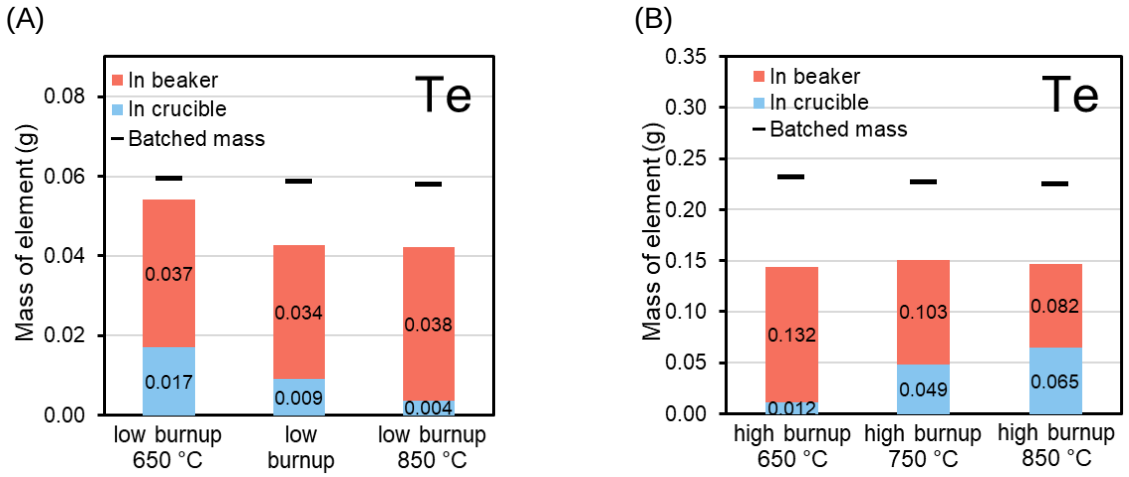

Figure 18: The total measured mass of tellurium in the crucible and in the beaker compared to the total batched mass for tests conducted using the (A) low and (B) high burnup salt.

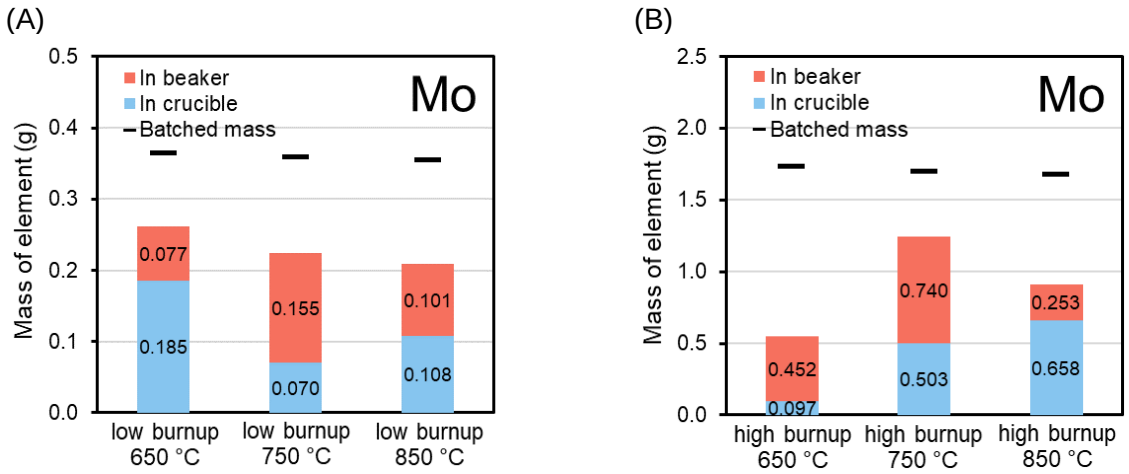

Figure 19: The total measured mass of molybdenum in the crucible and in the beaker compared to the total batched mass for tests conducted using the (A) low and (B) high burnup salt.

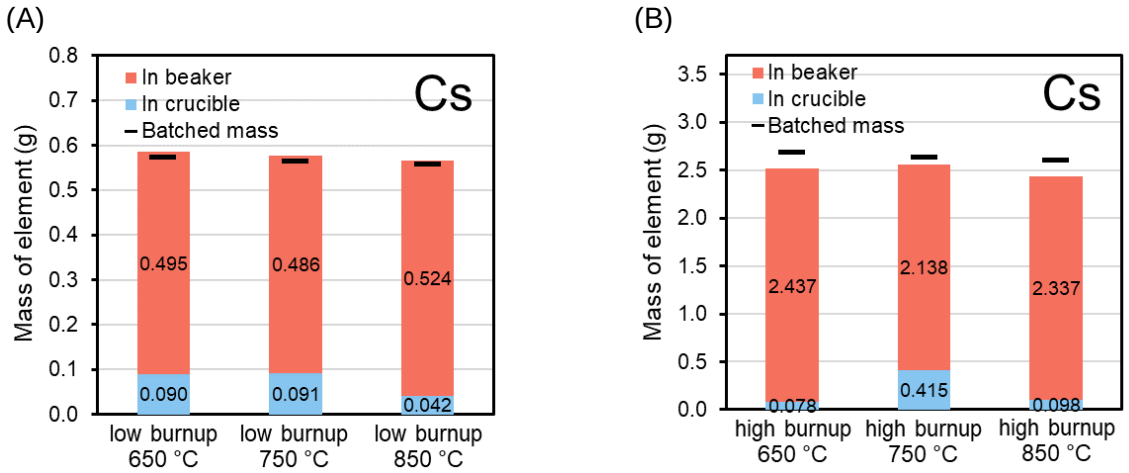

Figure 20: The total measured mass of cesium in the crucible and in the beaker compared to the total batched mass for tests conducted using the (A) low and (B) high burnup salt.

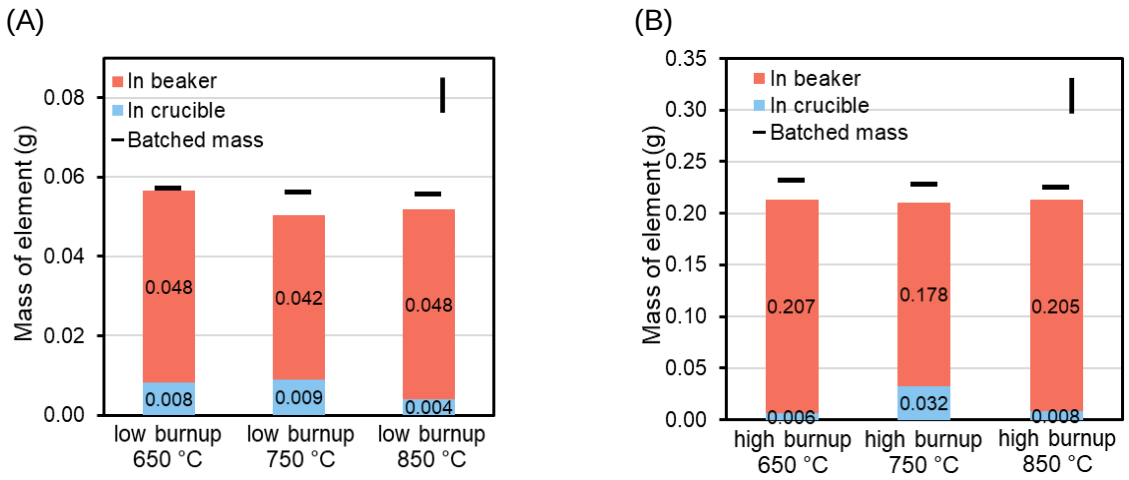

Figure 21: The total measured mass of iodine in the crucible and in the beaker compared to the total batched mass for tests conducted using the (A) low and (B) high burnup salt.

In contrast, the total recovered mass of tellurium and molybdenum in the salt after testing with both the low and high burnup salt compositions is consistently lower than the total batched mass (Figure 18 and Figure 19). The total recovered mass of cerium and neodymium is also lower than the total batched mass in tests conducted using the high burnup salt composition (Figure 15B and Figure 16B). A fraction of the tellurium and molybdenum could have been lost to vaporization during heating in the furnace, however loss to vaporization is not likely the sole cause for the significant difference in batched and recovered mass of tellurium and molybdenum after each test. Vaporization of cerium and neodymium also does not explain the partial recovery of these elements for tests conducted using the high burnup salt composition because these elements were nearly fully recovered after the tests conducted using the low burnup salt composition. It is more likely that only partial recovery of tellurium, molybdenum, cerium, and neodymium after testing occurs due to these elements not being fully dissolved in the salt mixture. Separate phases containing these elements floating on top of the molten salt could have been directly released to the atmosphere during spilling, contributing to the low concentrations of these elements measured in the frozen salt that was collected from the beaker after testing. Separate phases containing these elements in the frozen salt may not have been completely homogenized after the frozen salt was ground into a powder and may have been excluded from samples taken for composition analysis. It is also possible that some tellurium, molybdenum, cerium, and neodymium species partitioned to the crucible or beaker walls, which would decrease the concentration of these elements in the frozen salt that was collected for composition analysis and used to perform the mass balance.

5.8 Composition of aerosols collected on filters

Aerosol cassettes with 0.45-µm pore size PTFE filters connected to a sampling pump set to a constant flow rate of 4 L min^{-1} were used to sample the spill containment box atmosphere for suspended particulates (e.g., aerosols). The atmosphere of the spill containment box was sampled for approximately 20 minutes during each test. The aerosol cassettes were weighed before and after sampling using an analytical balance (Mettler Toledo Balance XPR226DR), and the total mass of particulates collected on each filter is presented in Figure 22. A new and unused filter blank was also weighed at the same time as the control and sample filters to confirm the accuracy of the balance. The two control filters in Figure 22 represent samples of the glovebox atmosphere within the spill containment box collected for 20 minutes after all testing had been completed to

provide a particulate background composition of the glovebox atmosphere. The controls were run after all testing had been completed as opposed to prior to all testing to provide a particulate background composition of the glovebox atmosphere that was representative of the conditions present during salt spill testing (i.e., exposed to powders of frozen crushed salt). Each control filter collected a similar mass of particles as the sample filters, suggesting that the glovebox atmosphere contains dust that was collected currently with the aerosols generated from the molten salt during testing. The particulate mass collected on the filter during the test with the high burnup salt composition at 650 °C was much higher than the mass collected during other tests (Figure 22). The loss of some non-dissolved surrogate fission product additives directly to the atmosphere during spilling, as suggested in Section 5.7, could explain the higher measured particulate mass measured in this test. The compositional analyses of the particulate material collected on filters during each spill test provides more insight into the origin of the collected particulate material to distinguish between background dust and salt.

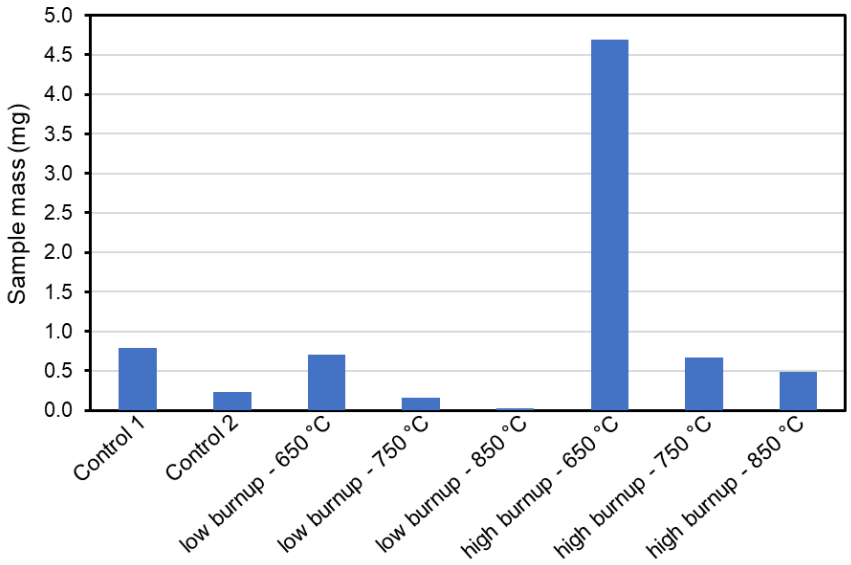

Figure 22: Mass of particulates collected on filters for tests conducted with the low and high burnup salt composition at target initial temperatures of 650 °C, 750 °C, and 850 °C.

The results of compositional analyses of particulates collected on the filters during each test with the low and high burnup salt composition are provided in Table 12. The only elements detected on the filters were cesium, iodine, tellurium, molybdenum, and ruthenium. No elements of interest were detected on the Blank or Control filters (Table 12). The amount of ruthenium measured by using ICP-MS after dissolution in aqueous solution may not be representative of the actual amount of ruthenium present on the filter due to incomplete dissolution of metallic ruthenium into aqueous solution. The mass of cesium and iodine collected on the filters after each test with both the low and high burnup salt composition increases with the initial temperature of the salt (Figure 23 and Table 12). In addition, the mass of cesium and iodine collected on the filters was greater for the tests conducted with the high burnup salt than those conducted with the low burnup salt at the same initial salt temperature (Figure 23 and Table 12). That the total amounts of cesium and iodine collected as particulates depend on the initial salt temperature indicates that the primary cesium- and iodine-bearing aerosol formation mechanism is vaporization and condensation. A similar trend with the initial salt temperature was observed during previous tests conducted at a smaller scale with FLiNaK doped with CsF and CsI (Thomas and Jackson, 2021).

More tellurium and molybdenum were collected on the filters during the tests conducted with the high burnup salt composition than during tests conducted with the low burnup salt composition. An increase in collected particulate mass with increasing initial salt temperature is not observed for tellurium and molybdenum as had been observed for cesium and iodine (Table 12). Notably, the amount of molybdenum collected on the filters was highest for the tests conducted at 650 °C and decreased with increasing initial salt temperature for both salt compositions. This trend can be explained by non-dissolved molybdenum spilling directly into the atmosphere, as had been suggested based on the mass balance assessment in Section 5.7. Both the low and high burnup salt compositions were collected after the first test at 650 °C and reused to conduct the next tests at 750 °C and 850 °C; therefore, each subsequent spill test at the higher temperature was likely conducted with a salt that had a smaller amount of non-dissolved molybdenum that was able to spill directly into the atmosphere. This also explains why the total particulate mass on the aerosol collection filter was highest for the test conducted at 650 °C using the high burnup composition (Figure 22).

Table 12: Elemental composition of particulates collected on 0.45 µm filters[a,b]

Composition	Initial salt temp. (°C)[c]	Cs (µg)	I (µg)	Te (µg)	Mo (µg)	Ru (µg)
Blank[d]	n/a	< 0.01	< 0.005	< 0.02	< 0.01	< 0.01
Control 1[e]	n/a	< 0.01	< 0.005	< 0.02	< 0.01	< 0.01
Control 2[e]	n/a	< 0.01	< 0.005	< 0.02	< 0.01	< 0.01
Low burnup	650	0.19	0.04	0.13	17.5	< 0.01
Low burnup	750	0.20	0.06	0.11	1.54	< 0.01
Low burnup	850	0.47	0.18	0.12	< 0.01	< 0.01
High burnup	650	0.65	0.13	2.15	501	0.17
High burnup	750	0.59	0.24	0.48	84.8	< 0.02
High burnup	850	2.07	0.37	0.37	9.51	< 0.01

[a] The number following the < is the detection limit.
[b] The following elements were below the detection limit on all tested filters (detection limit in parentheses): Li (0.13 µg), Na (0.09 µg), Mg (0.24 µg), Si (75 µg), K (6.8 µg), Ca (110 µg), Cr (0.20 µg), Fe (3.8 µg), Ni (0.02 µg), Cu (0.05 µg), Sr (0.01 µg), Zr (0.02 µg), Ce (0.02 µg), and Nd (0.02 µg).
[c] The initial salt temperature was estimated by using a thermocouple placed in the furnace liner in which the salt was heated.
[d] The composition of the blank filter was measured directly after removal from its packaging.
[e] The control filter sampled the background glovebox atmosphere for 20 minutes at the conclusion of all testing of the low and high burnup salt compositions.

Tellurium detected on the aerosol collection filters after tests with the high burnup salt displayed the same behavior as the molybdenum, where the mass of collected particulate tellurium was highest after the first test run at an initial salt temperature of 650 °C and decreased with subsequent tests run using the same salt. This suggests that non-dissolved tellurium also spilled directly into the atmosphere. The mass of particulate tellurium detected on the aerosol collection filters was approximately the same after each test conducted with the low burnup salt composition. The total recovered mass of tellurium after each test with the low burnup salt composition was more consistent with the batched mass than the total recovered mass of tellurium after testing with the high burnup salt composition (Figure 18). For these reasons, the source of the particulate tellurium measured on the aerosol collection filters after the tests with the low burnup salt composition may be the salt that had spilled into the beaker rather than direct release into the

atmosphere. Major salt components (sodium, potassium, and lithium) and some suspected fully or partially dissolved surrogate fission products (zirconium, cerium, and neodymium) were not detected on the aerosol collection filters after any test (Table 12). This suggests that mechanical breakup of the salt was not a major aerosol formation mechanism for the specific spill conditions that were tested herein.

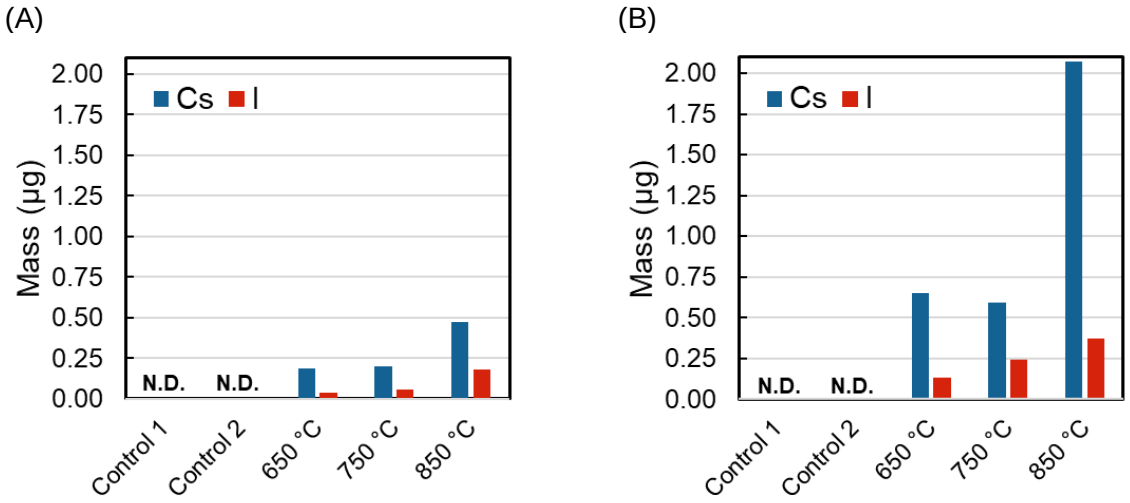

Figure 23: The mass of cesium and iodine detected on the aerosol collection filters as a function of the initial salt temperature for tests conducted with the (A) low burnup FLiNaK and (B) high burnup FLiNaK.

In summary, the mechanism for molybdenum and tellurium release from the molten salt during the spill tests likely involves non-dissolved molybdenum and tellurium species that float on the molten salt surface spilling directly into the atmosphere. This type of release mechanism of non-dissolved species should be considered in salt spill accident analyses, but the occurrence is likely highly dependent on the spill conditions. In contrast, the particulate cesium and iodine collected on the filters during testing were likely released from the molten salt pool in the beaker due to vaporization and condensation. The masses of cesium and iodine that became aerosolized and were collected on the filters are between six and seven orders of magnitude lower than the total cesium and iodine mass in the spilled salt (compare the results presented in Table 12 with those in Figure 20 and Figure 21). This mass fraction of cesium and iodine released from spilled molten salt as aerosol particles can be used to predict the cesium and iodine source term for spill scenarios like those tested herein. However, larger scale spills for which the salt is expected to remain molten for longer durations may release an even larger mass fraction of cesium and iodine than what was observed in these laboratory scale tests. Future tests are planned at larger scales to investigate the effect of the scale of the spill on aerosol release to provide additional data to support MSR licensing (Thomas, 2023). A mass transport code to predict the mass of cesium and iodine released from FLiNaK as vapors was developed and is described in Section 6. The results were compared to the measured mass of cesium and iodine on the aerosol collection filters from these tests to determine if the observations are supported by vapor mass transport and condensation into aerosol particles.

5.9 Size and composition of splatter and aerosol particles

Figure 24 provides a bird's eye view of the stainless steel beaker, the thermocouples immersed in the spilled salt, and the coupons to collect splatter and aerosol particles that were used in integrated process tests. All coupons had areas of approximately one square inch. The coupons

used to collect splatter were positioned near the mouth of the beaker. The coupon used to collect aerosol particles was positioned directly under the aerosol collection filter with the goal of capturing suspended particles from the gas stream. It is possible that some splatter particles may have reached the coupon intended to collect aerosol particles (i.e., particles that traveled due to the force of mechanical breakup and not due to their suspension in the gas stream). Figure 25 and Figure 26 provide secondary electron SEM micrographs and EDS spot analysis spectra of representative salt splatter particles collected on coupons during tests conducted at 850 °C with the low burnup and high burnup salt composition, respectively. The EDS results are not quantitative due to the surface topography of the particles but indicate the presence of elements with atomic numbers greater than five and at concentrations higher than a few weight percent. Lithium has atomic number of three and cannot be detected by using EDS.

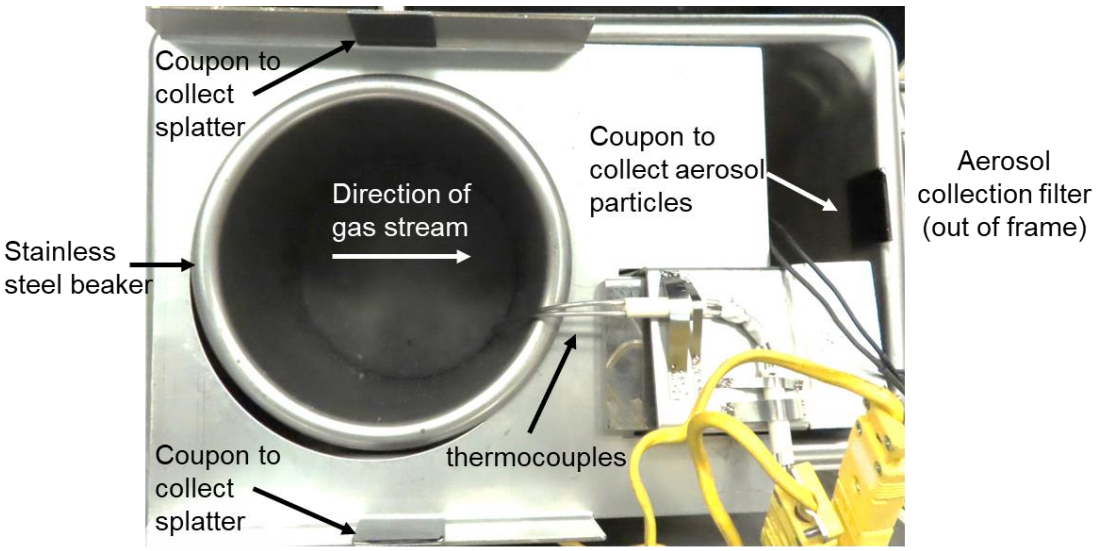

Figure 24: Bird's eye view of the stainless steel beaker, salt-immersed thermocouples, and the locations of the coupons to collect splatter and aerosol particles. The filter for aerosol collection is positioned directly above a coupon on the far wall from the beaker into which salt was spilled and is connected to a pump set to a constant flow rate of 4 L min^{-1}.

The projected diameter of the salt particles on the coupons are approximately 20 µm and 35 µm in Figure 25A and Figure 26A, respectively. High intensity peaks at characteristic X-ray emission energies of fluorine, sodium, and potassium in the EDS spectra in Figure 25B and Figure 26B confirm that both particles are primarily composed of FLiNaK. The source of the carbon and oxygen in the EDS spectra can be attributed to the carbon tape background. Oxygen could have been introduced to the salt particles while the coupons were exposed to air (i.e., humidity) during transfer into the SEM instrument. Air exposure occurred for less than two minutes for all samples. The EDS spectra of both particles show the presence of magnesium, aluminum, silicon, sulfur, and chlorine, all of which could have been impurities in the FLiNaK salts that were synthesized. Magnesium, aluminum, and silicon were not detected in salt samples that were analyzed by using ICP-MS. The magnesium, aluminum, silicon, sulfur, and chlorine could have also been components of dust particles present in the glovebox atmosphere that were simultaneously collected with and possibly attached to salt particles. Isolated dust particles having similar sizes as salt particles but composed of elements that were not included in the batched salt composition were observed in some regions of some coupons.

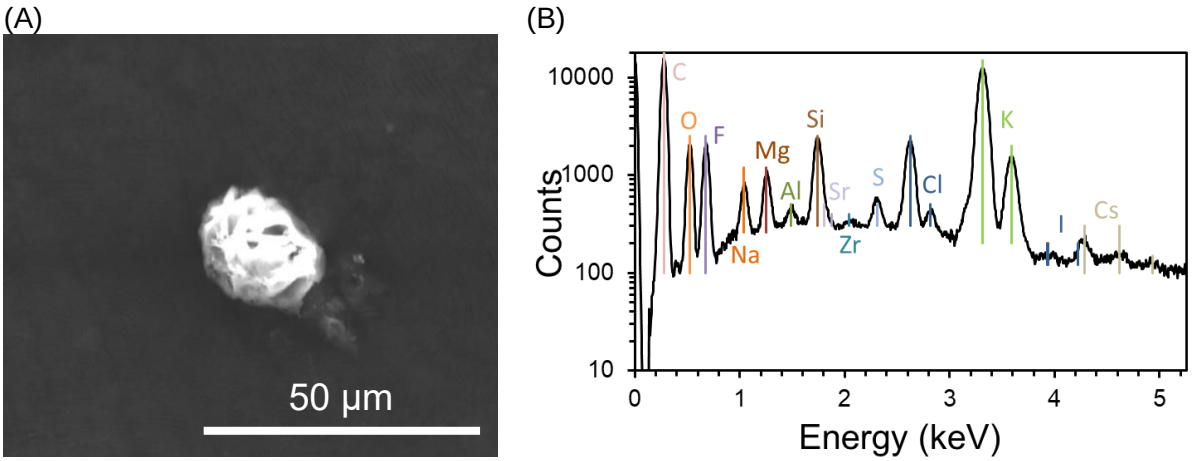

Figure 25: (A) Secondary electron micrograph and (B) EDS spectrum of a single splatter particle collected during the test with low burnup FLiNaK at an initial temperature of 850 °C.

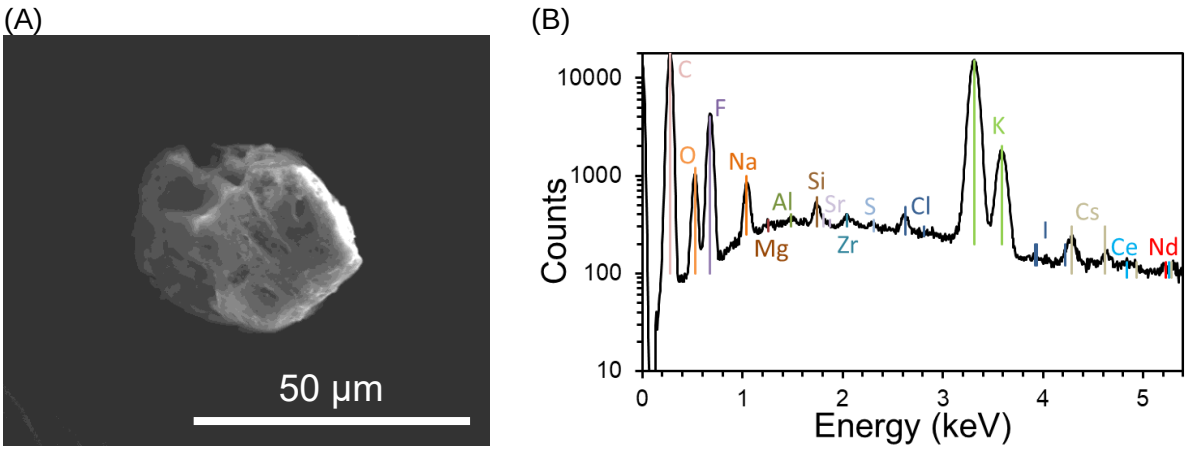

Figure 26: (A) Secondary electron micrograph and (B) EDS spectrum of a single splatter particle collected during the test with high burnup FLiNaK at an initial temperature of 850 °C.

The zirconium, cesium, and iodine surrogate fission products are present in both splatter particles from tests with the low and high burnup salt composition (Figure 25B and Figure 26B). Cesium and neodymium are also present in the splatter particle from test with the high burnup salt (Figure 26B). These surrogate fission products were partially or completely dissolved in the bulk salt (see Section 5.7) and their presence in collected splatter particles indicates that the salt splatter composition reflects the composition of the dissolved fraction of the salt. Additional splatter particles of similar size (10 to 40 µm projected diameter) and similar composition to the particles in Figures 25 and 26 were detected. Splatter particles with compositions drastically different from the batched salt composition could have formed during testing but were not detected.

Multiple small particles (< 20 µm projected diameter) primarily composed of sodium, potassium, and fluorine were detected on the coupon positioned to collect aerosol particles from the gas stream flowing through the aerosol collection filter. A secondary electron SEM micrograph and associated EDS spectrum of a particle with a projected diameter of approximately 15 µm that is primarily composed of the main constituents of FLiNaK are shown in Figure 27. This specific particle was collected during the test with the low burnup salt composition that was spilled at an initial temperature of approximately 850 °C. The fact that the composition of these particles is

similar to the bulk salt composition suggests that some small particles may form by a physical process such as mechanical breakup due to salt impaction on the catch pan or bubble bursting. But, the condensation of potassium- and sodium-bearing vapors to form the particle in Figure 27 cannot be ruled out.

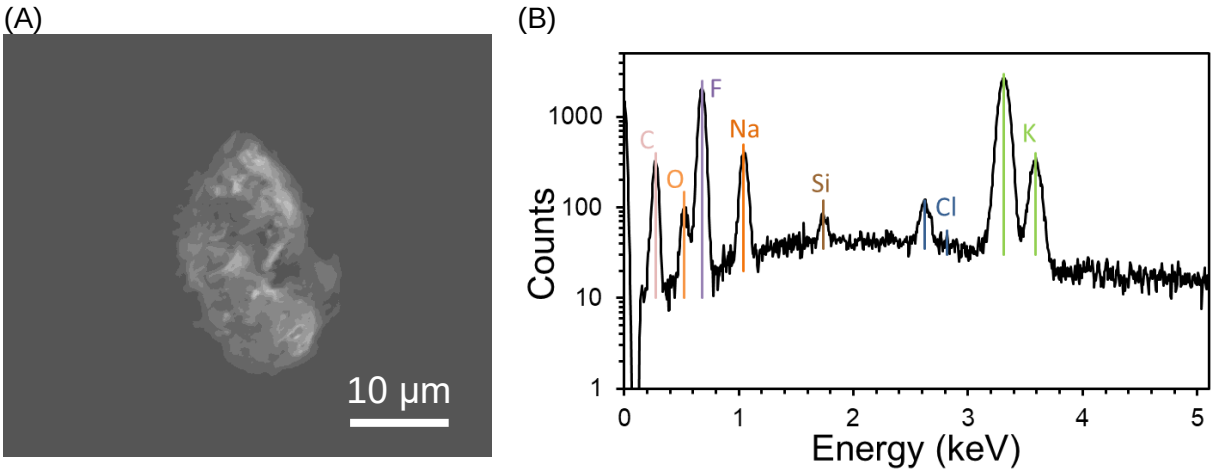

Figure 27: (A) Secondary electron micrograph and (B) EDS spectrum of a salt particle collected on the coupon below the aerosol collection filter during the test with low burnup FLiNaK at an initial temperature of 850 °C.

Small particles with high surrogate fission product content relative to base salt content were also collected on the coupon positioned below the aerosol collection filter during salt spill tests. The relative amounts of elements present in different particles were assessed by comparing the ratios of peak intensities in EDS spectra. For example, the relative amount of cesium and potassium in two different samples can be determined by comparing the ratio of the intensities of the cesium and potassium peaks in each EDS spectrum. Figure 28A shows a secondary electron micrograph of an aerosol particle with a projected diameter of about 5 µm that was collected during the test with the low burnup salt that was spilled at an initial temperature of 850 °C. The EDS spectrum collected for this particle has peaks at X-ray emission energies characteristic of base salt elements sodium, potassium, and fluorine and peaks at energies characteristic of surrogate fission product elements strontium, zirconium, and cesium (Figure 28B). The ratio of intensities of the zirconium and cesium peaks to the intensities of the sodium and potassium peaks in the EDS spectrum in Figure 28B are relatively high when compared to the same ratios in the EDS spectra of salt splatter particles (Figure 25B and Figure 26B). This indicates that the particle shown in Figure 28 has a higher cesium and zirconium content relative to potassium and sodium content than the splatter particles in Figure 25A and Figure 26A.

A rectangular shaped particle with a length of approximately 5 µm and a primary composition of zirconium was detected on the coupon below the aerosol filter during the test with the high burnup salt at an initial temperature of approximately 850 °C, and a secondary electron micrograph of this particle is shown in Figure 29A. The EDS spectrum of this particle shows it also contains some fluorine, strontium, molybdenum, and potassium (Figure 29B). Because the composition of this particle is so different from the bulk salt composition, its formation mechanism is likely different than that of the particles with compositions that resemble the bulk salt. A zirconium-rich phase present in the molten salt prior to spilling could have broken up into aerosol particles during the spill test due to a physical process such as bubble bursting. Alternatively, metallic zirconium vapor could have condensed in the atmosphere with vapors of other species (e.g., KF and SrF_2) to form the particle observed in Figure 29.

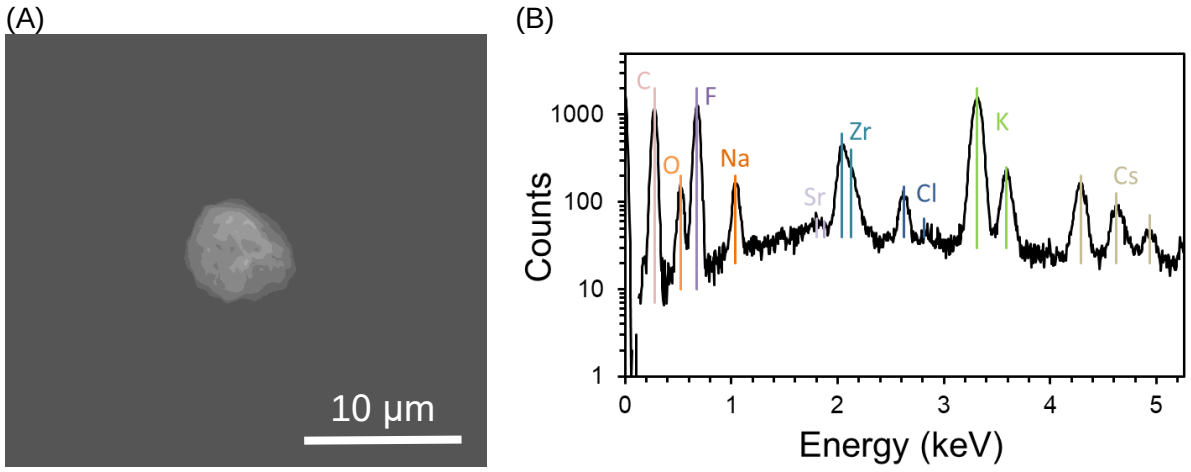

Figure 28: (A) Secondary electron micrograph and (B) EDS spectrum of a particle collected on the coupon below the aerosol collection filter during the test with low burnup FLiNaK at an initial temperature of 850 °C.

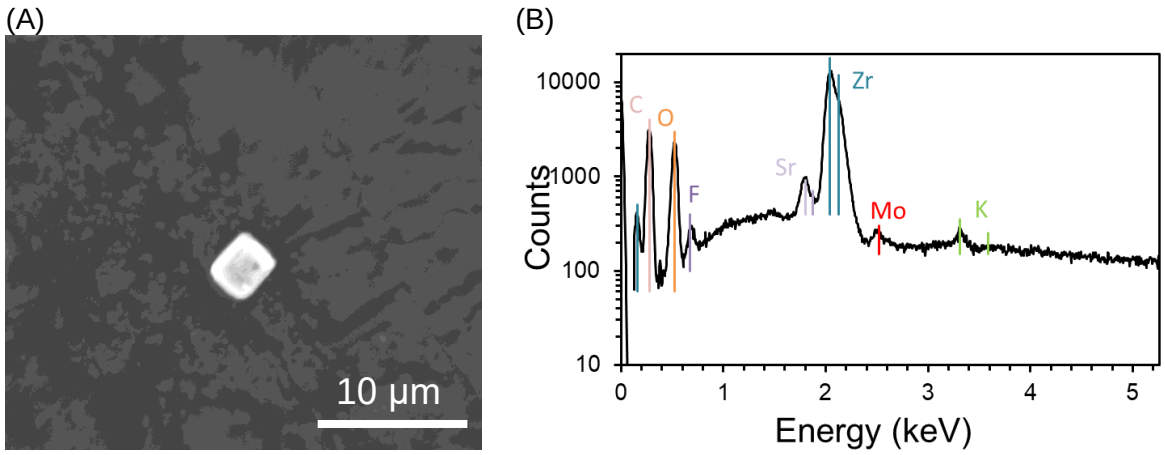

Figure 29: (A) Secondary electron micrograph and (B) EDS spectrum of a particle collected on the coupon below the aerosol collection filter during the test with high burnup FLiNaK at an initial temperature of 850 °C.

In summary, the results from SEM-EDS analysis of splatter and aerosol particles collected on coupons provides insight into the sizes of particles generated during spill tests and the compositions of these particles. One limitation of this technique for aerosol analysis is that it requires manual assessment of individual aerosol particles collected on adhesive; particles with other compositions may have formed during testing that were not analyzed. The development of a method for monitoring the real-time generation of salt aerosol particles during spill tests will provide more quantitative characteristics of the global population of aerosols formed over time.

6 Application of thermodynamic and mass transport modeling to provide insight into aerosol formation mechanism

The potential mechanisms for aerosol formation during a molten salt spill accident include the mechanical breakup of molten salt upon impact on the catch pan, the bursting of bubbles at the surface of the molten salt pool, and vaporization and condensation (Shahbazi et al., 2022). An

analysis of the elemental composition results of particulates on the aerosol collection filters provided in Section 5.8 shows that the salt-soluble and relatively volatile elements cesium and iodine are detected, while the main salt components (i.e., sodium, lithium, and potassium) are not detected. In addition, the amount of cesium and iodine detected as particulates on the filters increases with increasing initial salt temperature. These observations suggest that the main cesium- and iodine-bearing aerosol formation mechanism is vaporization and condensation. Aerosol formation by mechanical breakup or bubble bursting would not likely yield such strong temperature-dependent aerosol composition results.

A mass transport modeling approach was taken using the vapor pressures of cesium and iodine species above FLiNaK to compare the predicted total mass of cesium and iodine released from the salt surface as vapor species to the measured masses of cesium and iodine collected as particulates on the aerosol collection filters (Table 12). The test system (salt and atmosphere of spill containment box) likely did not reach equilibrium by the time the molten salt surface froze, so the vapor pressures of these species alone are not sufficient to compare with measured aerosol composition results. The rate of vapor species transport from the salt surface to the atmosphere must also be considered. A schematic of the mass transport model of the salt spill test system that was used to predict the time-dependent release of cesium and iodine vapor species from FLiNaK is shown in Figure 30. The arrows represent vaporization of unspecified species (Figure 30).

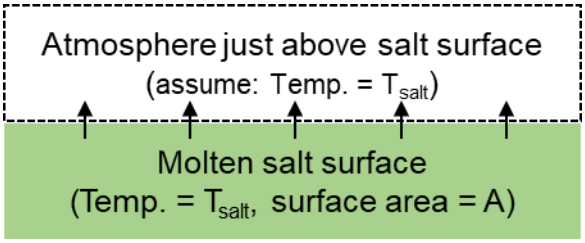

Figure 30: Schematic of cesium and iodine vapor mass transport model of salt spill test system.

The total mass of cesium and iodine released as vapor species from the molten salt surface to the atmosphere over the duration the salt surface was molten was calculated by solving Equation 1:

$$\frac{dm_i}{dt} = Ak_i\left(C_i^{Sat} - C_i^a\right) \quad (1)$$

where m_i is the mass of species i (grams), A is the area of the salt surface (m^2), k_i is the mass transfer coefficient of species i in an argon atmosphere (m s^{-1}), C_i^{Sat} is the saturation concentration of species i in the atmosphere just above the salt surface (g m^{-3}), and C_i^a is the concentration of species i in the atmosphere just above the salt surface (g m^{-3}). The C_i^a changes with time as the m_i also changes with time. The model assumes that the salt surface and gas atmosphere right above the salt surface are at the same temperature and that C_i^{Sat} is given by the vapor pressure of species i at the temperature of the salt surface.

The mass transport model was created using the following assumptions:

1) Vapor release ceases when the molten salt surface freezes.
2) All cesium and iodine vapor species released from the salt surface condense in the atmosphere and form aerosol particles due to the large temperature gradient between the salt surface (Figure 9) and the atmosphere (Figure 12, Figure 13, Figure 14).

3) The vapor release rate of cesium and iodine species over the duration that the salt surface is molten can be estimated from the initial modeled vapor release rate. This is described in more detail below (Figure 32). We assumed that the vapor release rate follows the initial calculated vapor release rate over the duration that the salt surface is molten. This assumption accounts for the decrease in vapor concentration in the atmosphere above the salt surface due to venting of the atmosphere through the aerosol collection filter and the condensation of vapors into aerosol particles.

It is important to note that these assumptions were applied to the specific molten salt spill scenario evaluated in the tests described in this report to gain insight into the aerosol formation mechanism of cesium- and iodine-bearing aerosols. These assumptions are not necessarily recommended to predict radionuclide release for other scenarios.

The vapor pressures of cesium and iodine species above FLiNaK as a function of salt temperature were calculated using the Molten Salt Thermal Properties Database-Thermochemical Version 2.0 (MSTDB-TC V2.0) (Ard et al., 2022). For simplicity, the salt composition for the vapor pressure calculations consisted of only cesium, iodine, and the components of FLiNaK (i.e., sodium, potassium, lithium, and fluorine). The vapor pressure calculations assumed a salt composition of CsF and CsI mixed with stoichiometric FLiNaK. The masses of cesium, iodine, and FLiNaK used in the vapor pressure calculations were determined from the measured masses of each element in the recovered salt in the beaker and the total mass of salt recovered after each spill test. These masses of cesium and iodine were converted to masses of CsF and CsI so that the salt in the thermodynamic model would have a similar redox potential as the salt used in the spill tests, while maintaining the same total mass of cesium and iodine. The salt composition used for the vapor pressure calculations for each test is provided in Table 13. The vapor pressures of cesium- and iodine-bearing species calculated using the MSTDB-TC V2.0 and the low burnup salt composition at 650 °C reported in Table 13 are shown as a function of temperature in Figure 31.

Table 13: Salt composition (g) for thermodynamic modeling of species vapor pressures

Salt component	Low burnup at 650 °C	Low burnup at 750 °C	Low burnup at 850 °C	High burnup at 650 °C	High burnup at 750 °C	High burnup at 850 °C
CsF	0.508	0.506	0.541	2.538	2.232	2.425
CsI	0.099	0.085	0.098	0.424	0.364	0.420
LiF	79.336	76.127	83.767	89.485	75.922	85.488
NaF	31.760	30.476	33.534	35.824	30.394	34.223
KF	160.496	154.005	169.459	181.028	153.589	172.942

The calculated vapor pressures ($P_i^{Sat}(T)$; atm) were converted to the saturation concentrations (C_i^{Sat}; g m^{-3}) in the gas right above the salt surface using the following equation:

$$C_i^{Sat} = \frac{P_i^{Sat}(T) M_i}{RT} \quad (2)$$

where M_i is the molecular weight of species i (g mol^{-1}), R is the ideal gas constant (8.2057 × 10^{-5} m^3 atm mol^{-1} K^{-1}), and T (K) is the temperature of the salt surface. The salt surface and the gas just above the salt surface are assumed to be at the same temperature. The measured temperature of the salt surface decreased with time after the salt was spilled into the beaker. Linear

functions of salt surface temperature versus time were created using the initial salt surface temperature, the average surface temperature at freezing, and the duration the salt surface was molten. These values are provided for each test in Table 14. The temperature of the salt surface was measured by using an IR camera and the temperature results were not corrected for the emissivity of the salt, which has not yet been determined. For this reason, the salt surface temperatures reported in Table 14 are likely lower than the actual surface temperatures. Nonetheless, the determination of the duration that the salt surface remained molten from temperature measurements made by an IR camera is not affected by these unknown salt emissivities. The saturation concentrations of each species in the atmosphere above the salt surface change with time after the spill because the salt surface temperature and hence the vapor pressures of species also change with time.

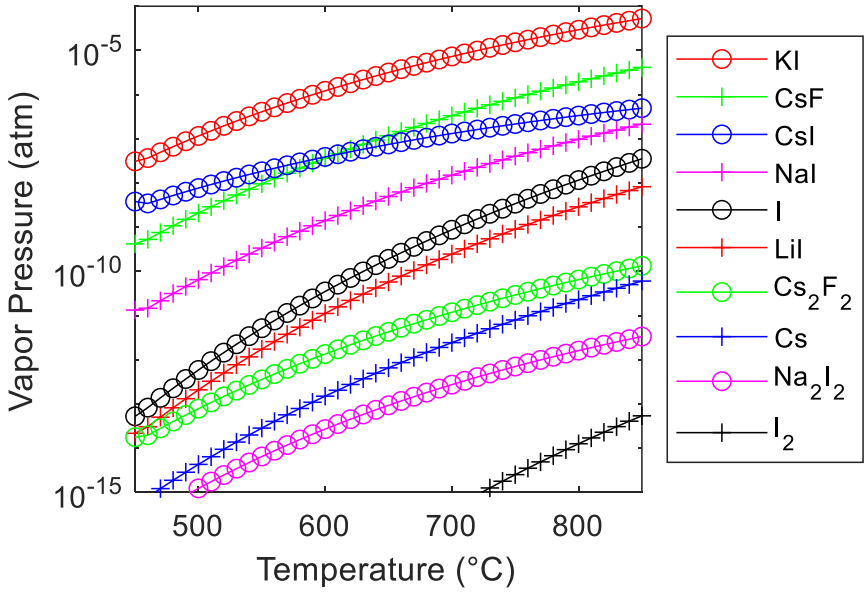

Figure 31: The ten cesium- and iodine-bearing species with the highest calculated vapor pressures above FLiNaK for the salt composition from the test conducted with low burnup FLiNaK at an initial temperature of 650 °C.

Table 14: Time for the molten salt surface to freeze and average surface temperature at freezing

	Low burnup at 650 °C	Low burnup at 750 °C	Low burnup at 850 °C	High burnup at 650 °C	High burnup at 750 °C	High burnup at 850 °C
Molten surface duration (min)[a]	3.15	6.10	8.85	4.00	6.58	9.53
Avg. surface temp. (°C) at freezing[b]	426	389	417	395	360	367
Initial salt temperature (°C)	592	685	786	538	663	779

[a] The duration that the surface was molten was taken as the time to reach the temperature at which the phase change from liquid to solid occurs.
[b] The temperature was averaged over the entire salt surface and was measured by using an IR camera. The temperature is not corrected for the emissivity of the salt, which is unknown.

The mass of species i released from the salt surface due to vaporization as a function of time was solved using Equation 1 and the ordinary differential equation solver *ode45* in MATLAB®. Only KI, CsF, and CsI were considered as vapor species in the mass transport calculation because the calculated vapor pressures of those species in Figure 31 indicate that they will be the dominant Cs- and I-bearing species being released from the salt as a vapor. Mass transfer coefficients of KI, CsF, and CsI in argon gas were fixed and were not calculated using assumptions as had been done in Kalilainen et al. (2020). Fixing the mass transfer coefficients allowed for multiple calculations to be performed using different values to see the effect those values had on mass release from the salt surface.

Removal of KI, CsF, and CsI vapors from the atmosphere just above the salt surface to other regions of the atmosphere will occur due to their transport in the gas stream that flows towards the aerosol collection filter and their condensation into aerosol particles. For this reason, the concentrations of KI, CsF, and CsI vapors in the region of the atmosphere just above the salt surface are not expected to reach their saturation concentrations. As such, the mass release rates of KI, CsF, and CsI vapors from the molten salt surface are not expected to approach zero over time. To provide a conservative estimate of vapor release rate that accounts for the continuous removal of vapor species from the region in the atmosphere just above the salt surface, the mass release rate of vapors from the salt surface was assumed to follow the initial mass release rate for each species for the duration that the salt surface was molten. This is depicted in Figure 32 for the example of CsI vapor release from FLiNaK that was calculated using the conditions of the test with low burnup FLiNaK at an initial temperature of 650 °C.

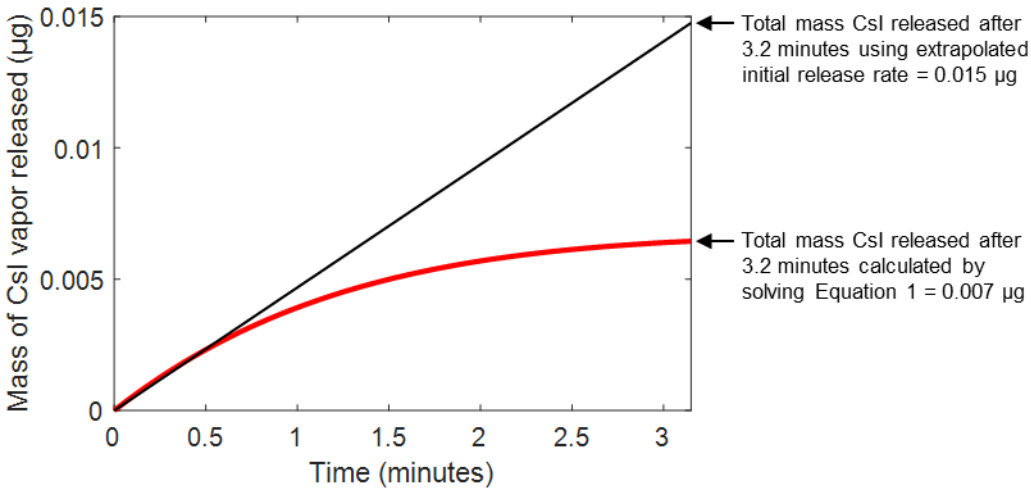

Figure 32: Calculated accumulated mass of CsI released from FLiNaK for the salt composition used in tests with the low burnup FLiNaK at an initial temperature of 650 °C (fixed k_{CsI} = 0.005 m s^{-1}). The red line shows the mass of CsI released over time by solving Equation 1 and the black line shows the mass of CsI released over time that was calculated by extrapolating the initial mass release rate over the duration the salt surface was molten.

Mass transport calculations were performed for various fixed mass transfer coefficient values for species KI, CsF, and CsI, and the total mass of cesium and iodine released from FLiNaK over the duration the salt surface was molten for each test conducted is presented in Table 15. The calculations predict cesium and iodine mass release within one to two orders of magnitude of the measured particulate mass of cesium and iodine detected on filters for each test. Possible reasons

for the predicted mass release being different from the mass of particulate cesium and iodine measured on the aerosol collection filters include:

- The particle collection efficiency on the filter likely being less than 100%,
- The model assumption that all released cesium and iodine vapor species condense to form aerosols,
- Uncertainties associated with the vapor pressures calculated by using the MSTDB-TC,
- The assumption that the gas phase layer immediately above the salt surface was the same temperature as the salt surface,
- The use of fixed mass transport coefficients of KI, CsF, and CsI in argon that do not change as a function of temperature, and
- The calculation of saturation vapor pressures using temperatures measured by an IR camera that were not corrected for salt emissivity.

Table 15: Calculated mass of Cs and I released (µg) for each test conducted[a]

	Element	Low burnup at 650 °C	Low burnup at 750 °C	Low burnup at 850 °C	High burnup at 650 °C	High burnup at 750 °C	High burnup at 850 °C
Calculation 1 k_{CsF} = 1 mm s^{-1} k_{CsI} = 1 mm s^{-1} k_{KI} = 1 mm s^{-1}	Cs	0.003	0.022	0.15	0.016	0.16	0.95
	I	0.041	0.32	1.9	0.071	1.1	7.5
Calculation 2 k_{CsF} = 5 mm s^{-1} k_{CsI} = 5 mm s^{-1} k_{KI} = 5 mm s^{-1}	Cs	0.013	0.11	0.74	0.078	0.78	4.8
	I	0.20	1.6	9.3	0.36	5.3	38
Calculation 3 k_{CsF} = 5 mm s^{-1} k_{CsI} = 1 mm s^{-1} k_{KI} = 1 mm s^{-1}	Cs	0.007	0.083	0.64	0.022	0.34	2.9
	I	0.041	0.32	1.9	0.071	1.1	7.5
Measured on filters	Cs	0.19	0.2	0.47	0.65	0.59	2.07
	I	0.04	0.06	0.18	0.13	0.24	0.37

[a] The mass transfer coefficient (k) of each species used in each calculation is listed below the calculation number.

The calculations do show a strong dependence of the total mass of cesium and iodine released on the initial temperature of the salt, which captures the observed behavior from the aerosol measurements. All calculations predict higher masses of iodine released than masses of cesium released (Table 15). This prediction does not agree with the composition results for particulates collected on filters, where more cesium was consistently detected than iodine. No combination of realistic mass transfer coefficients used in the calculations produced results with a higher cesium mass released than iodine. More iodine was released than cesium even when the mass transfer coefficient of CsF was set to a value 5 times higher than that of CsI and KI (Calculation 3, Table 15). This result is likely related to the fact that the calculated vapor pressure of KI is much higher than that of CsF above FLiNaK (Figure 31). It is notable that potassium was not detected on the aerosol collection filter for any test, which would be expected if the dominant iodine species

released from the salt was KI. The detection limit of potassium for the method used is approximately 7 µg (Table 12); therefore, it is possible that the amount of potassium present on the filters was below this detection limit. If KI was in fact the dominant vaporizing iodine-bearing species, the amounts of potassium that would correspond to the measured amounts of iodine on the aerosol collection filters are well below the potassium detection limit of 7 µg.

In summary, the mass transport model for vapor release from molten salt pools and subsequent condensation in cooler atmospheres does capture the temperature dependence of the total mass of cesium and iodine present as aerosol particles measured in the salt spill tests. This mass transport model for predicting species vaporization and condensation from static pools of molten salt will be developed further as new measurements are made and the accuracy of vapor pressures calculated by using the MSTDB-TC is improved.

7 Accomplishments and summary of key findings

Integral effects tests on molten salt spill accidents were conducted at a laboratory scale using two salt compositions to provide experimental data on the coupling between the thermohydraulic behavior of the molten salt and the dispersal of surrogate fission products. The two salt compositions were composed of eutectic FLiNaK as the base salt with different concentrations of surrogate fission products to represent fuel salts with different burnups. The major accomplishments of this work include:

- Assessing recently reported depletion calculation results done for the MSRE to identify relevant surrogate fission product concentrations that represent MSRs and would provide insight into the dispersal behavior of source term-significant radionuclides.
- Generating data to support the development of models on heat transfer from static molten salt pools and aerosol generation due to spills of radionuclide-bearing molten salt.
- Applying the methods and measurement techniques that were previously developed during individual process tests to integrated process tests and gaining experience in measuring several processes simultaneously to facilitate conducting integral effects tests at an engineering scale.
- Demonstrating new test methods to provide real-time measurements of the flow rate of a liquid spilling onto a catch pan and the real-time size quantification of aerosols in an argon atmosphere (as described in Appendix A).
- Developing a mass transport model for cesium and iodine vapor release from molten salt pools to provide insight into the cesium- and iodine-bearing aerosol formation mechanism observed during testing.

The main findings from the integral effects tests conducted with two compositions of FLiNaK containing surrogate fission products are as follows:

- The high burnup salt composition appears to have a lower emissivity than the low burnup salt composition. This was determined by comparing the melting temperatures measured by the IR camera (which are affected by emissivity) and the measured melting temperatures obtained using thermocouples (which are not affected by emissivity).

- A significant radial temperature gradient was not observed at the salt surface while the two molten salt compositions cooled in the beaker after the spill as had been observed during previous heat transfer studies with FLiNaK and eutectic NaCl-UCl_3 (Thomas and Jackson,

2022). This is likely because the walls of the beaker were insulated for the tests conducted herein and were not insulated during the previous tests, which would impact heat loss from the salt to the beaker walls.

- The temperature plateau in the cooling curve representing the liquid salt to solid salt phase change that was measured at the beaker underside surface during each spill test provides a good estimate of the salt melting temperature. The beaker underside temperature reached the same temperature as the salt with which it had direct contact during the phase change because the beaker base and walls were insulated and minimal heat was lost from the beaker base.

- The temperature of the atmosphere measured during each spill test remained relatively low compared to the temperature of the salt that was spilled. The maximum recorded temperature among all tests was approximately 73 °C, which was measured at the top of the spill containment box.

- The concentrations of surrogate fission products were measured in the salt that remained in the crucible after spilling and in the salt that spilled into the beaker. Similar concentrations that were measured in salt samples from both locations indicated that the surrogate fission products were completely dissolved in the salt prior to spilling. This comparison indicated that CeF_3, NdF_3, ZrF_4, CsF, and CsI were completely dissolved in the low burnup salt composition and that ZrF_4, CsF, and CsI were completely dissolved in the high burnup salt composition. The other surrogate fission products likely existed as separate solid phases that either settled to the bottom of the crucible or floated on the salt surface before spilling.

- The only elements detected on the aerosol collection filters were cesium, iodine, tellurium, molybdenum, and ruthenium. The masses of cesium- and iodine-bearing particulates collected on the filters showed a strong dependence on the initial salt temperature, which suggests an aerosol formation mechanism of vaporization and subsequent condensation in cooler regions of the atmosphere. The masses of molybdenum and tellurium in tests with the high burnup salt composition and the masses of molybdenum in tests with the low burnup salt composition that were detected on the aerosol collection filters were highest for the first test that was conducted and decreased after each subsequent test with the same salt composition. This dependence on the order that the tests were conducted indicates that some molybdenum and tellurium that was not dissolved in the salt was released directly into the atmosphere during spilling.

- Splatter particles collected on coupons near the mouth of the beaker during salt spill tests and analyzed by using SEM-EDS ranged in size from 10 to 40 μm projected diameter and had compositions that reflected the completely dissolved components of the salt (i.e., sodium, potassium, fluorine, zirconium, cesium, and iodine). Neodymium and cerium were detected in some salt splatter particles collected during tests with the high burnup salt composition.

- Small particles (< 20 μm projected diameter) composed mainly of FLiNaK constituents were detected on the coupon intended to collect aerosol particles. The formation mechanism of these particles is unknown but likely involved a physical process such as mechanical breakup due to contact with the catch pan floor or bubble bursting.

- Small particles (< 10 μm projected diameter) with high contents of surrogate fission products (i.e., zirconium, strontium, and cesium) relative to base salt components (i.e., sodium and potassium) were collected on the coupon positioned below the aerosol collection filter during salt spill tests. The formation mechanism of these particles is likely vaporization and condensation because their compositions differ significantly from the composition of the bulk salt that was spilled into the beaker. It is also possible that the components of these particles were present in the molten salt as separate phases from the bulk liquid that were released as aerosol particles during the spill test due to physical processes such as bubble bursting.

- A mass transport model was developed using the assumption that cesium and iodine are released from the molten salt pool as vapor species that subsequently condense into aerosol particles after transport to cooler regions of the atmosphere. This model predicts the mass of cesium and iodine in particulates collected on filters during testing within one to two orders of magnitude and accounts for the dependence of mass release on initial salt temperature that was observed experimentally. The mass transport model will improve as the thermodynamic database used to calculate the vapor pressures of cesium and iodine species is developed.

- Experimental measurements of vapor pressures and aerosol formation in molten salt systems are needed to improve mass transport models of radionuclide release from molten salts as vapors and aerosols.

References

Ard, J. C., Yingling, J. A., Johnson, K. E., Schorne-Pinto, J., Aziziha, M., Dixon, C. M., et al. (2022). "Development of the Molten Salt Thermal Properties Database−Thermochemical (MSTDB−TC), Example Applications, and LiCl−RbCl and UF_3−UF_4 System Assessments." *Journal of Nuclear Materials, 563*, 153631.

Bostelmann, F., Skutnik, S. E., Walker, E. D., Ilas, G., and Wieselquist, W. A. (2022). "Modeling of the Molten Salt Reactor Experiment with SCALE." *Nuclear Technology, 208*(4), 603-624.

Fei, T., Shahbazi, S., Fang, J., and Shaver, D. (2022). "Validation of Neams Tools Using MSRE Data." Argonne National Laboratory report ANL/NSE-22/48.

Gardner, L., and Rose, M. A. (2023). "Property Measurements of NaCl-UCl_3 and LiF-NaF-KF Molten Salts Doped with Surrogate Fission Products." Argonne National Laboratory report ANL/CFCT-23/23.

Gelbard, F., Beeny, B. A., Humphries, L. L., Wagner, K. C., Albright, L. I., Poschmann, M., et al. (2023). "Application of MELCOR for Simulating Molten Salt Reactor Accident Source Terms." *Nuclear Science and Engineering*, 1-19.

Humphries, L., Beeny, B., Louie, D., Esmaili, H., and Salay, M. (2018). "Non-LWR Model Development for the MELCOR Code." Sandia National Laboratories report SAND2018-0297C.

Kalilainen, J., Nichenko, S., and Krepel, J. (2020). "Evaporation of Materials from the Molten Salt Reactor Fuel under Elevated Temperatures." *Journal of Nuclear Materials, 533*, 152134.

Leute, J., Beeny, B., Gelbard, F., and Clark, A. (2021). "Identification and Resolution of Gaps in Mechanistic Source Term and Consequence Analysis Modeling for Molten Salt Reactors Salt Spill Scenarios." Sandia National Laboratory report SAND2021-15350.

Lo, A., Bostelmann, F., Hartanto, D., Betzler, B., and Wieselquist, W. A. (2022). "Application of SCALE to Molten Salt Fueled Reactor Physics in Support of Severe Accident Analyses." Oak Ridge National Laboratory report ORNL/TM-2022/1844.

McMurray, J. W., Johnson, K., Agca, C., Betzler, B. R., Kropaczek, D. J., Besmann, T. M., et al. (2021). "Roadmap for Thermal Property Measurements of Molten Salt Reactor Systems." Oak Ridge National Laboratory report ORNL/SPR-2020/1865.

Rader, D., Brockmann, J., Ceman, D., and Lucero, D. (1990). "A Method to Employ the Aerodynamic Particle Sizer Factory Calibration under Different Operating Conditions." *Aerosol science and technology, 13*(4), 514-521.

Shahbazi, S., and Grabaskas, D. (2021). "A Pathway for the Development of Advanced Reactor Mechanistic Source Term Modeling and Simulation Capabilities." Argonne National Laboratory report ANL/NSE-21/21.

Shahbazi, S., Thomas, S., Kam, D. H., and Grabaskas, D. (2022). "State of Knowledge on Aerosols and Bubble Transport for Mechanistic Source Term Analysis of Molten Salt Reactors." Argonne National Laboratory report ANL/NSE-22/47.

Thomas, S. (2023). "Conceptual Design of Engineering-Scale Molten Salt Spill Tests to Support Molten Salt Reactor Licensing." Argonne National Laboratory report ANL/CFCT-23/13.

Thomas, S., and Jackson, J. (2021). "Testing to Evaluate Processes Expected to Occur During MSR Salt Spill Accidents." Argonne National Laboratory report ANL/CFCT-21/22.

Thomas, S., and Jackson, J. (2022). "MSR Salt Spill Accident Testing Using Eutectic NaCl-UCl_3." Argonne National Laboratory report ANL/CFCT-22/32.

Appendix A: New measurement techniques for molten salt spill tests

A.1 Real-time aerosol particle size and concentration measurement using Aerodynamic Particle Sizer

Systems analysis codes such as MELCOR require real-time aerosol particle generation measurements during individual and integrated effects tests to validate the modeled aerosol release rates and size distributions for possible accident scenarios, including molten salt spills. A recent report on the application of MELCOR for predicting the source terms of MSR accidents specifically mentions the need for experiments that use aerosol monitoring instrumentation based on light scattering and aerodynamic particle sizing to quantify the mass and rate of aerosol release during simulated accident scenarios (Gelbard et al., 2023). Aerosol particle sizing instrumentation has been extensively applied to monitor aerosol generation in ambient air atmospheres for applications including environmental monitoring and the pharmaceutical industry. This type of aerosol monitoring has not yet been applied to monitor aerosols that are generated under the conditions of a molten salt spill accident, which may have high-temperature and non-air atmospheres (Shahbazi et al., 2022). In addition, aerosol particles composed of salts may behave differently than the traditional particle standards used for instrument calibration; the successful application of aerosol particle sizing instrumentation may require calibration with standard particles that have similar properties (e.g., density) as salt aerosol particles.

Instrumentation that measures the aerodynamic particle diameter (as opposed to the actual particle diameter) provides the true airborne behavior of the particle and is the preferred property for aerosol transport modeling (Shahbazi et al., 2022). Commercially available instrumentation can detect a size range between 0.5 μm and 20 μm aerodynamic diameter but has a maximum operating temperature of approximately 40 °C. Employing commercial instrumentation to monitor aerosols generated from molten salts in laboratory experiments would likely require the dilution of the gas stream carrying the aerosol particles with a cooler gas to maintain the temperature within operating specifications.

Another potential issue with employing commercial instrumentation to monitor aerosols under conditions that are relevant to MSR accidents is that all available commercial instrumentation is intended for use in air atmospheres. Some MSRs intend to use an inert gas in the reactor containment building and aerosol generation rates in inert atmospheres should be quantified experimentally to provide relevant data for accidents that occur in inert atmospheres.

We tested the functionality of the Aerodynamic Particle Sizer® from TSI Inc. in an air and argon gas atmosphere using standard particles (polystyrene latex spheres) to determine 1) if the factory-calibrated instrument would provide signal in an argon atmosphere and 2) to compare the measured aerodynamic particle sizes in air and argon atmospheres. A demonstration Aerodynamic Particle Sizer® unit was installed in a benchtop glovebag filled with ultra-high purity argon gas to test the functionality of the instrument in argon. The results of the test in an air and argon atmosphere using standard aerosol particles is summarized in Figure A-1. The Aerodynamic Particle Sizer® functions in an argon atmosphere and provides a relatively accurate measure of the nominal aerosol aerodynamic diameter for 1 μm and 5 μm aerodynamic diameter particles without the need for a correction factor (Figure A-1). The factory-calibrated instrument did not accurately measure the nominal aerodynamic diameter of the 10 μm particles in either the air or argon atmosphere. A correction factor to account for effects such as non-Stokesian drag, for example, can be applied to obtain accurate measurements for larger particles (Rader et al., 1990). Applying this instrument to measure the aerodynamic sizes of salt particles would require

a similar calibration as was performed here but with particles having similar properties as salts. The use of the Aerodynamic Particle Sizer® to provide real-time particle concentrations in the gas stream would require a mass flow controller attachment to provide an accurate mass flow rate of inert gas.

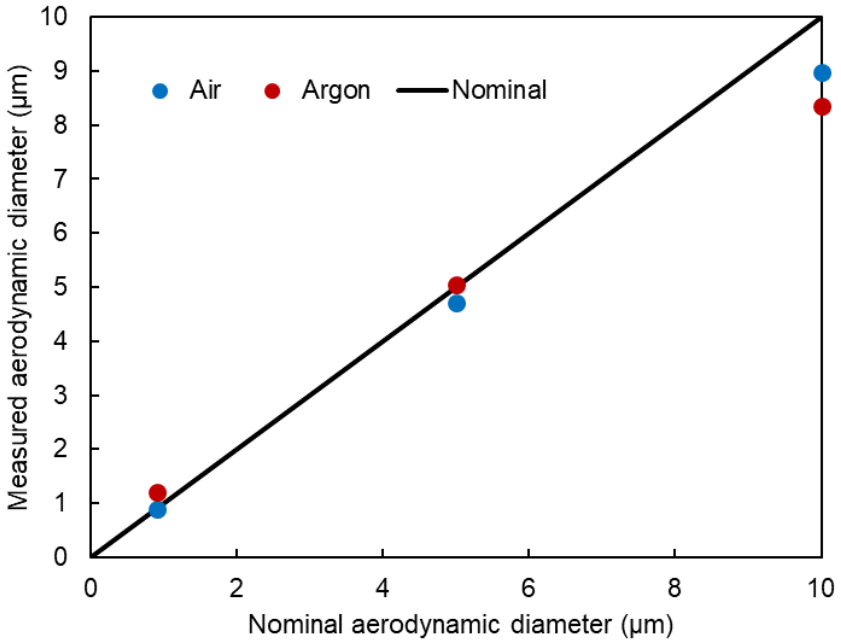

Figure A-1: The average measured aerodynamic diameter of standard aerosol particles in an air and argon atmosphere.

A.2 Monitoring liquid spill rate using a data-logging balance

Monitoring the mass flow rate of molten salt onto a catch pan in molten salt spill tests will be beneficial to the quantification of accident consequence because it can provide a measure of the force of impact (i.e., the velocity) of the spilled molten salt onto the catch pan over the duration of the spill. The known spill velocity over time can be correlated with quantified processes such as the molten salt aerosol generation rate to develop correlations in accident analysis codes. We tested the accuracy of using a data-logging balance (Mettler Toledo MS32001L/03) to measure the mass of water spilling at a known flow rate to determine whether this method would be appropriate to measure the mass flow rate of spilled molten salt. A known mass (and volume) of deionized water at room temperature was spilled from a funnel with known orifice diameter to control the mass flow rate of the water spill. The funnel orifice was approximately 2 cm above the base of the catch pan that was placed on the balance. The data logging balance measured the mass of water being collected in the catch pan placed on the data logging balance at 0.083 second intervals. The theoretical mass of water impinging onto a catch pan placed on the data logging balance was calculated using the Bernoulli equation. The theoretical, measured, and average mass of water collected on the catch pan over time is presented in Figure A-2. The average mass of water spilled was calculated using the final mass of water in the catch pan and the duration of the spill. Notably, there is an approximately 0.1 second lag between the time the water actually spills into the catch pan and when the balance records an initial increase in mass (Figure A-2). The measured mass then oscillates around the theoretically calculated mass and more closely

agrees with the theoretically calculated mass than the mass determined from the average spill rate. These results suggest that a data-logging balance will be able to reasonably measure the mass flow rate of spilled molten salt in planned experiments. The benefit of this measurement will be more pronounced for spill scenarios that have highly variable mass flow rates throughout the spill duration (i.e., much higher initial flow rates than terminal flow rates), where the average mass flow rate will not be able to capture the time-dependent variation.

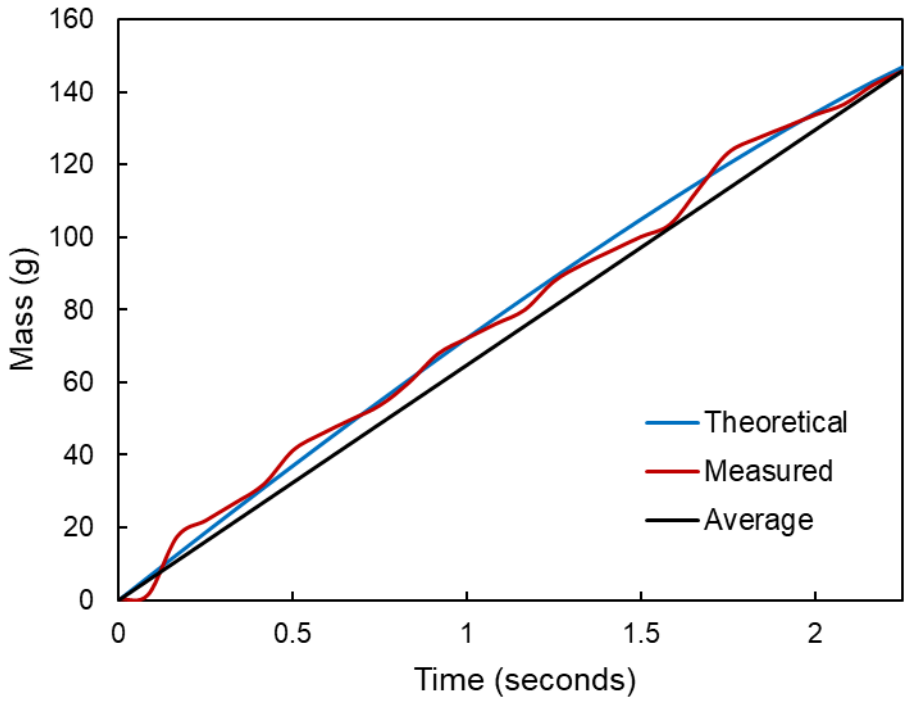

Figure A-2: The measured, theoretical, and average mass of water collected in the catch pan placed on the data logging balance.

Chemical and Fuel Cycle Technologies Division
Argonne National Laboratory
9700 South Cass Avenue, Bldg. 205

Argonne, IL 60439

www.anl.gov